Fluctuations and dissipation in a Bose-Einstein condensed photon gas

Dissertation
zur
Erlangung des Doktorgrades (Dr. rer. nat.)
der
Mathematisch-Naturwissenschaftlichen Fakultät
der
Rheinischen Friedrich-Wilhelms-Universität Bonn

von
Fahri Emre Öztürk
aus
Diyarbakır, Türkei

Bonn, 16.09.2021

Angefertigt mit Genehmigung der Mathematisch-Naturwissenschaftlichen Fakultät der Rheinischen Friedrich-Wilhelms-Universität Bonn

1. Gutachter:	Prof. Dr. Martin Weitz
2. Gutachter:	Prof. Dr. Sebastian Hofferberth
Tag der Promotion:	22.11.2021
Erscheinungsjahr:	2021

Abstract

Bose-Einstein condensation, superfluidity and superconductivity are all related phenomena where particles behave as collective quantum systems. The behavior of such systems is treated using quantum statistics and their properties such as energy distribution or coherence are used to describe the system at a macroscopic level. These quantities are affected not only by the intrinsic features of the particles that constitute the quantum gas, but also by the interaction of these particles with their environment. The effect of a coupling of the quantum gas with its surroundings can be as drastic as completely changing its coherence properties or it might lead to a slight deviation from an equilibrium energy distribution. In this thesis, we investigate the effects caused by coupling a quantum gas of light with its environment.

Quantum gases of light are realized in optical microcavities filled with a medium the photons couple to. If a strong coupling between the light and the medium is realized, the gas comprises mixed states of matter and light such as polaritons. Phenomena like lasing, Bose-Einstein condensation and superfluidity can be observed in such systems. In the opposite case, when the coupling of medium and photons is weak, no coherent coupling is established and the gas consists of pure photons. The latter situation can be experimentally realized in high quality optical microcavities filled with photo-excitable dye molecules. In this system it was shown that if the lifetime of the photons in the cavity are sufficiently long, they thermalize at the temperature of the dye solution. And if the density of the photons is increased beyond a critical point, a Bose-Einstein condensate of photons forms.

A distinct feature of a condensate of photons in the dye-microcavity system compared to atom or polariton condensates is that the dye molecules act as a reservoir of particles, as well as energy. The photon gas exchanges particles with excited dye molecules and the coupling between the two is of statistical nature. It has been shown that Bose-Einstein condensation can coexist with unusually large particle number fluctuations in the so called grand-canonical statistical ensemble regime. In the first part of this thesis, we experimentally investigate the fluctuation-dissipation relation in a Bose-Einstein condensate of photons realized in the dye-microcavity. In equilibrium, thermally driven fluctuations are closely connected to how the system dissipates its excess energy or particles. This relation is so general that it has been observed in a variety of systems ranging from Brownian particles to quantum gases of atoms. However, its validity in Bose-Einstein condensates has not been shown. Despite being intrinsically in thermal equilibrium, fluctuations usually completely diminish in a Bose-Einstein condensate soon after the condensation threshold. We measure the second-order coherence of the photon Bose-Einstein condensate to search for the expected ratio of statistical number fluctuations and compressibility following the fluctuation-dissipation theorem.

Another intriguing aspect of the photon condensate is introduced due to the imperfect reflectivity of the cavity mirrors. In the second part of this thesis we show that this openness can lead to the existence of new states of the condensate. Physical models often consider systems that are completely isolated from their environment, such as a gas of particles closed in a box. Real-life situations often deviate from these idealized scenarios and the system loses energy or particles to its surroundings. In contemporary physics, systems which are dissipatively coupled to the environment are actively studied in a broad range of research fields ranging from optics to biophysics. Here, we investigate the open-system dynamics of a photon condensate in grand-canonical ensemble conditions. We identify non-Hermitian phases of the system that are observed by abrupt changes in the dynamics of the condensate's second-order coherence.

List of publications related to this thesis

1. F.E. Ozturk et al., Fluctuation dynamics of an open photon Bose-Einstein condensate, Physical Review A **100**, 043803, 2019. https://doi.org/10.1103/PhysRevA.100.043803

2. F.E. Öztürk et al., Observation of a non-Hermitian phase transition in an optical quantum gas, Science **372**, 88-91, 2021. https://doi.org/10.1126/science.abe9869

3. F. Öztürk et al., Phasen eines Bose-Einstein-Kondensats aus Licht: Photonenkondensat, Physik in unserer Zeit **52**, 162-163, 2021. https://doi.org/10.1002/piuz.202170404

4. F.E. Öztürk et al., Fluctuation-dissipation relations of a grand-canonical Bose-Einstein condensate, in preparation.

Contents

CHAPTER 1

Introduction

In a letter dated June 1924, a young physicist named Satyendra Nath Bose asked Einstein for assistance in arranging the publication of his new derivation of Planck's Law. In his work, Bose interpreted electromagnetic radiation as a quantum gas [1], which immediately caught the attention of Einstein. Moreover, Einstein soon realized that the same approach, applied to massive particles, also yields the quantum theory of the ideal gas [1, 2]. It was his conjecture that the analogy between a photon gas and an atomic gas is not a mere coincidence [2, 3]. In his 1925 paper, referring to Bose's work he notes that "If it is justifiable to conceive of radiation as a quantum gas, then the analogy between the quantum gas and a molecular gas must be a complete one" [3]. It is in this paper that Einstein predicts the phenomenon of Bose-Einstein condensation, though the nature of the condensation was so mysterious that he was sceptical whether his theory reflected reality. In a letter to Ehrenfest he writes "From a certain temperature on, the molecules "condense" without attractive forces, that is, they accumulate at zero velocity. The theory is pretty, but is there also some truth to it?" [2]. It would be seventy years for Bose-Einstein condensation to be observed in experiments where dilute atomic gases of rubidium and sodium were cooled to temperatures close to absolute zero [4–6].

Experimental realization of Bose-Einstein condensation led to a surge of activity in the study of quantum gases [6]. The macroscopic wavefunction of a condensate is directly observable, which opened the possibility of completely new ways of studying quantum phenomena [6, 7]. After ultracold atoms, Bose-Einstein condensates were realized also with exciton-polaritons, mixed states of matter and light [8, 9]. The condensation of bosons without any attractive force originates from the indistinguishability and the wave nature of particles. If conditions are realized so that the de Broglie wavelength of the particles (which can be understood as the position uncertainty related with their thermal momenta) are comparable to the inter-particle distance, the particles become indistinguishable [7]. At this point, bosonic particles occupy the same quantum state and form a coherent macroscopic wave. Bose-Einstein condensation was predicted by applying quantum statistical methods originally developed for photons to atoms. Coming back to the analogy between photons and atoms, if it is a complete one as Einstein had conjectured, the condensation phenomenon predicted for atoms should also apply to photons. Bose-Einstein condensation of photons is however, not observed in the example of blackbody radiation where the chemical potential always vanishes. But this restriction can be overcome, in optical microcavities filled with photo-excitable molecules. Fifteen years after the first observation of the condensation phenomenon in atoms, a Bose-Einstein condensate of photons was also observed [10–12] followed by other low-dimensional photon gas experiments [13–15]. In

Section 1.1 of this chapter we introduce the concepts that lead to the Bose-Einstein condensation of photons. An unusual characteristic of photon condensates is that the macroscopic wavefunction is not completely isolated from its environment. The effect of this open character is seen especially clearly with an investigation of the fluctuations in the condensate photon number. In this thesis, we measured these fluctuations as we systematically controlled the openness of the condensate to its surroundings. We continue this chapter by explaining the coupling of a photon condensate to a reservoir of particles in Section 1.2. This coupling can induce fluctuations as large as the condensate itself. Finally, in Section 1.3 we introduce the open-system dynamics of the photon condensate which originate from the residual photon losses. This openness leads to deviations from equilibrium observed in the dynamics of the fluctuations and ultimately to non-Hermitian phases of the photon gas.

1.1 Bose-Einstein condensation of photons in a dye-microcavity

In this section we give a concise theoretical description of the photon Bose-Einstein condensation phenomenon realized in a fluorescent dye filled optical microcavity. We highlight the role of stimulated emission, photon thermalisation and cavity confinement as well as the introduction of a non-vanishing chemical potential of photons. A thorough derivation of the statistical theory of the photon gas is given in references [16, 17]. We at this point simplify the calculations by neglecting the photon losses, hence describing an idealized photon box. In the experiments described in this thesis, the loss rate of the cavity is three orders of magnitude smaller than the thermalisation rate and no deviation from Bose-Einstein distribution was observed within experimental limits, justifying the simplified model we use here. The effect of mirror losses on the thermalisation process has been investigated in detail in earlier work [18, 19]. First, we write the rates of absorption and stimulated emission of photons by the dye molecules, which are equal in the case of a steady-state photon number in the cavity.

$$B_{\mathrm{abs}}\bar{M}_{\mathrm{g}}\bar{n}, \tag{1.1a}$$

$$B_{\mathrm{em}}\bar{M}_{\mathrm{e}}(\bar{n}+1). \tag{1.1b}$$

Here, $\bar{M}_{\mathrm{g}}$ and $\bar{M}_{\mathrm{e}}$ are the number of ground- and excited-state molecules and B_{abs} and B_{em} are Einstein coefficients for the rates absorption and stimulated emission, respectively. The bars denote an average over a time that is longer than the time scales of the cavity dynamics and the mean photon number in the cavity is indicated as $\bar{n}$. Writing the rates of absorption $B_{\mathrm{abs}}\bar{M}_g\bar{n}$ and stimulated emission $B_{\mathrm{em}}\bar{M}_e(\bar{n}+1)$ of radiation is so habitual for physicists that it is not uncommon to forget the underlying arguments that lead to this understanding. Here, $(\bar{n}+1)$ is a bosonic enhancement factor. It originates from the statistical tendency of identical bosons to occupy the same state [20]. The scattering of atoms to the ground state of the system during the formation of a Bose-Einstein condensate and the stimulated emission of photons during lasing are consequences of this statistical behavior of bosons [7]. In our calculation here, we try to reach the Bose-Einstein distribution using eqs. (1.1) as the starting point to illustrate the underlying bosonic enhancement effect that leads to Bose-Einstein condensation. Bose-Einstein condensation is special among equilibrium phase transitions that it does not require interparticle interactions; it is a purely quantum statistical phenomenon. The fact that a macroscopic occupation is reached by bosonic stimulation for both lasing and Bose-Einstein condensation highlights the connection between the two phenomena. In our experiments on Bose-Einstein condensation of photons, this connection is accessible and the investigation of it is a central

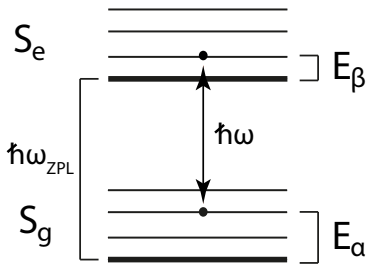

Figure 1.1: Rovibronically splitted energy levels of a two-level photo-excitable molecule. If the molecule is completely isolated from collisions with other molecules, the ground and excited states, S_{g} and S_{e} do not have additional substates and the only transition happens at the zero-phonon-line frequency ω_{ZPL}. With intermolecular collisions the molecule attains rotational and vibrational substates that are thermally populated [17].

theme in this thesis.

Note that the coefficients used here are rate coefficients for photon number and not for energy density. For a two-level dye molecule without the rotational and vibrational (rovibronic) substates, the Einstein coefficients for absorption and stimulated emission are equal. It is known since Einstein's work on the derivation of the blackbody radiation that the absorption and stimulated emission can be considered the same processes which are reversed [21]. However, in the case of collisions with the solvent molecules, the energy levels are subject to rovibronic splitting (Figure 1.1). In this case, the Einstein coefficients become an average over the pairs of substates α, β at the transition frequency ω [16, 17]. In this case we can write

$$\frac{B_{\mathrm{em}}}{B_{\mathrm{abs}}} = \frac{\sum\limits_{\alpha,\beta} p_\beta B(\beta \to \alpha)}{\sum\limits_{\alpha,\beta} p_\alpha B(\alpha \to \beta)}, \tag{1.2}$$

where $B(\alpha \to \beta)$ denote the Einstein coefficients for the transitions between individual substates. If the substates of each state S_{g} and S_{e} are thermally populated, the probabilities of finding the molecule in substates p_α and p_β are given with a Boltzmann factor.

$$p_\alpha = \frac{e^{-E_\alpha/k_{\mathrm{B}}T}}{\sum\limits_{\alpha} e^{-E_\alpha/k_{\mathrm{B}}T}}, \tag{1.3a}$$

$$p_\beta = \frac{e^{-E_\beta/k_{\mathrm{B}}T}}{\sum\limits_{\beta} e^{-E_\beta/k_{\mathrm{B}}T}}. \tag{1.3b}$$

Here, the sums in the denominators are the statistical weights of the states S_{g} and S_{e}. By assuming

equal statistical weights for the ground and excited states, we write

$$\frac{p_\beta}{p_\alpha} = e^{-(E_\beta - E_\alpha)/k_\mathrm{B}T}. \tag{1.4}$$

Applying the conservation of energy, we write the difference of substate energies E_α, E_β with the transition and zero-phonon line frequencies ω and ω_ZPL.

$$E_\alpha + \hbar\omega = \hbar\omega_\mathrm{ZPL} + E_\beta. \tag{1.5}$$

From (1.4) and (1.5) we obtain

$$p_\beta = e^{-\hbar(\omega - \omega_\mathrm{ZPL})/k_\mathrm{B}T} p_\alpha. \tag{1.6}$$

Plugging eq. (1.6) in eq. (1.2), and employing $B(\alpha \to \beta) = B(\beta \to \alpha)$ for each pair of α, β we write

$$\frac{B_\mathrm{em}}{B_\mathrm{abs}} = e^{-\hbar(\omega - \omega_\mathrm{ZPL})/k_\mathrm{B}T}. \tag{1.7}$$

Eq. (1.7) is known as the Kennard-Stepanov relation [22, 23]. It describes the thermalisation of the photon gas via absorption and emission of photons by the dye molecules. The rovibronic dye states S_g and S_e are thermalised as the dye molecules collide with the solvent molecules. Their thermalisation introduces a Boltzmann factor linking the substate probability distributions p_α, p_β, which is transferred to the spectral distribution of the photon gas with the absorption and emission processes [16, 17]. In this way, thermal equilibrium between the photons and the cavity medium (dye solution) is established.

Besides an energy exchange between the photons and the dye molecules which results in a thermal photon gas, there is also a particle exchange between the two species. Due to this particle exchange, the photon gas and the excited state molecules are in chemical equilibrium in the dye-microcavity if a steady state photon number is established [17]. In this case where the dye medium is constantly irradiated by the cavity photons, the difference between the chemical potentials of the ground and excited state dye molecules is written as [24]

$$\mu_\mathrm{e} - \mu_\mathrm{g} = \hbar\omega_\mathrm{ZPL} + k_\mathrm{B}T \ln\left(\frac{\bar{M}_\mathrm{e}}{\bar{M}_\mathrm{g}}\right), \tag{1.8}$$

where μ_e and μ_g are the chemical potentials of the excited and ground state dye molecules, respectively. In chemical equilibrium, the chemical potential of the photon gas, μ_γ satisfy the relation [16]

$$\mu_\gamma + \mu_\mathrm{g} = \mu_\mathrm{e}. \tag{1.9}$$

Using (1.8) and (1.9) we obtain

$$\frac{\bar{M}_\mathrm{e}}{\bar{M}_\mathrm{g}} = e^{(\mu_\gamma - \hbar\omega_\mathrm{ZPL})/k_\mathrm{B}T}. \tag{1.10}$$

Eq. (1.10) illustrates the meaning of the chemical potential in the dye-microcavity system. For the case when the excited state population is determined only by the thermal energy as in the case of blackbody radiation, the chemical potential is zero, $\mu_\gamma = 0$. For a photo-chemical reaction as described here, the molecules are under constant irradiation which adds an external non-vanishing chemical potential μ_γ to eq. (1.10) (Figure 1.2). The photons that are added to the cavity externally

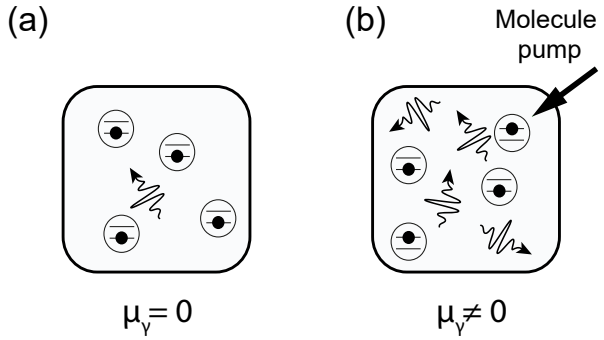

Figure 1.2: A perfectly reflective cavity filled with two-level, photo-excitable molecules. (a) When the molecules are not externally excited, the number of photons is only adjusted by the thermal energy. The chemical potential μ_γ vanishes. (b) When the molecules are pumped externally, the number of excited molecules is altered and this adds an energy offset which corresponds to a non-vanishing chemical potential.

alter the excited state population and hence the chemical potential [24]. In this way, an external pump laser that excites the dye molecules is a control parameter for the chemical potential of the photon gas in our experiments. In general, the chemical potential can be described using different parameters such as internal energy or concentration [25]. In our calculations, we described the chemical potential using the number of the excited state molecules. Therefore, the physical effect of a changing chemical potential is a diffusion of the particles between the photon gas and the molecular excitations. However, this is not a diffusion in spatial coordinates as the molecules and the photons share the same space.

The absolute value of the chemical potential depends on where we define the zero value of the potential energy [25]. In the experiments, the cavity introduces a low frequency cutoff ω_c, which determines the ground-state energy $\hbar\omega_\mathrm{c}$ (see Figure 1.3). We renormalize the chemical potential by removing this ground-state energy, $\mu = \mu_\gamma - \hbar\omega_\mathrm{c}$. We then define the dye-cavity detuning, $\Delta = \omega_\mathrm{c} - \omega_\mathrm{ZPL}$ to write eq. (1.10) in the following form which we will use in Chapter 2 [16].

$$e^{\mu/k_\mathrm{B}T} = \frac{\bar{M}_\mathrm{e}}{\bar{M}_\mathrm{g}} e^{-\hbar\Delta/k_\mathrm{B}T}. \tag{1.11}$$

For a steady-state photon number we equate the terms (1.1) and write $\frac{M_\mathrm{e}}{M_\mathrm{g}}\frac{B_\mathrm{em}}{B_\mathrm{abs}} = \frac{\bar{n}}{\bar{n}+1}$. We plug (1.7) and (1.10) in this relation and solve for $\bar{n}(\omega)$, which gives the Bose-Einstein distribution for the photon gas

$$\bar{n}(\omega) = \frac{1}{e^{(\hbar(\omega-\omega_\mathrm{c})-\mu)/k_\mathrm{B}T} - 1}. \tag{1.12}$$

The photon energies are therefore Bose-Einstein distributed in the cavity with a non-vanishing photon chemical potential, but that alone is not sufficient to achieve condensation in our experiments. Note that the critical photon number for Bose-Einstein condensation does not converge for the distribution given in eq. (1.12). In the experiments, a thermalised gas of photons that follow the Bose-Einstein distribution is prepared in an optical microcavity that is filled with photo-excitable dye molecules. Figure 1.3 illustrates the optical microcavity and the allowed energy levels of the harmonic

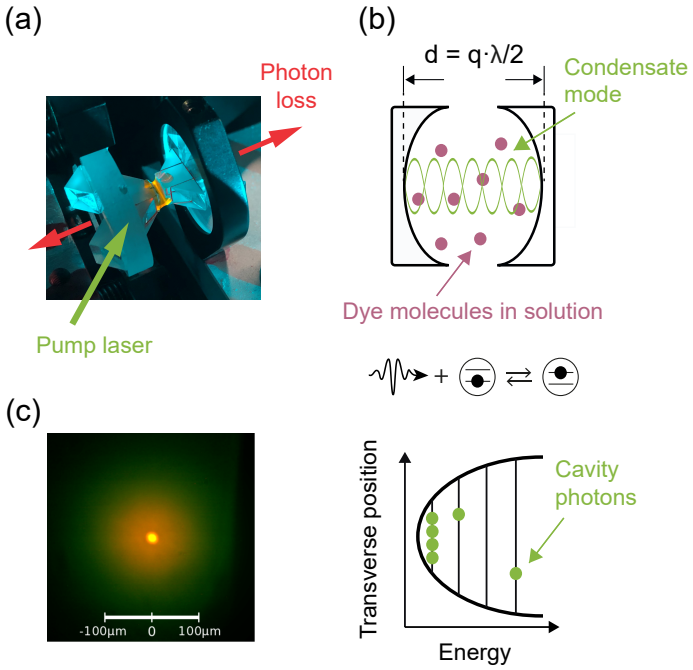

Figure 1.3: (a) A photograph of the photo-excitable dye filled optical microcavity used in the experiments. Prisms glued to one of the mirror substrates are used to couple-in the pump beam. The ultra-high quality mirrors have reflectivities of about 99.998%. Nevertheless their imperfection causes a residual loss of photons through the mirror transmission. (b) Schematic of the dye-filled cavity and the condensate mode for the fixed longitudinal mode number of $q = 7$. The exchange of molecular excitations and photons can be written as a chemical reaction. The total number of photons and molecular excitations are conserved in the cavity. The mirrors are spherical with radii of curvatures of 1 m. This induces a harmonic trapping potential for the confined photons. (c) An image of the photon condensate taken from the cavity emission [10]. When the intensity of the pump laser is increased the number of photons reach a critical point. The populations of all cavity modes except the ground mode saturate and the condensate forms as a bright spot at the cavity center.

potential induced by its curved mirrors, $u = 0, \hbar\Omega, 2\hbar\Omega...$, where Ω is the trapping frequency and $u = \hbar\omega - \hbar\omega_c$ is a renormalized photon energy where we set the ground-state of the system at $u = 0$. The mirrors are separated by a short distance of only 7 half-wavelengths which correspond to approximately 1.5 μm. When the mirrors are so close, only photons of a single longitudinal mode occupy the cavity. This means that the longitudinal dimension freezes and the photon energies are thermally distributed to the remaining two transverse modes. Therefore, the photon gas becomes two-dimensional. The degeneracy for the energy levels of the two-dimensional harmonic potential is written as $g(u) = 2(\frac{u}{\hbar\Omega} + 1)$. Here, the factor of 2 correspond to the two-fold polarization degeneracy [17]. It follows that under harmonic confinement, the critical number of photons for Bose-Einstein condensation converges in the limit of $\mu \to 0$ with $\bar{n}_c = \sum_{u=\hbar\Omega,2\hbar\Omega...} \frac{g(u)}{e^{u/k_B T}-1}$ which yields [17]

$$\bar{n}_c = \frac{\pi^2}{3}\left(\frac{k_B T}{\hbar\Omega}\right). \tag{1.13}$$

Once this critical photon number is reached in the cavity, the thermal photon cloud saturates. Every new photon added beyond this critical value goes into the ground state of the cavity. In the experiments we observe this phenomenon as a bright emission at the cavity center, where the ground-state (TEM_{00} mode) photons accumulate at. A broad emission distributed to higher energy levels (transverse modes) following the thermal equilibrium Bose-Einstein distribution is also observed [10]. Figure 1.3(c) shows a spatial image of the photon gas. A condensate is seen as a bright yellow spot at the cavity center. The rest of the cavity photons comprise the thermal cloud. Due to the harmonic trapping, the cavity emission has a color gradient moving from yellow (lower energetic photons) at the trap center to green (higher energetic photons) at outer regions of the cavity.

The last point we would like to emphasise in this section is that the reflectivities of the mirrors are high enough to assume a perfect photon box for our current purpose; i.e. to demonstrate the Bose-Einstein distribution and the critical number of photons for condensation. Both of these quantities are static, they are averaged over a time that is much longer than the timescales relevant for the dynamical quantities of the cavity such as the loss rate. Our experiments lead to the understanding that the static quantities such as energy distribution, critical photon number for Bose-Einstein condensation and entropy agree with the expected behavior from thermal equilibrium within experimental limits [10, 18, 26, 27]. In Chapter 2 of this thesis we investigate the fluctuation-dissipation relations with time-averaged quantities that are time-independent at the steady state. Within the scope of this thesis we further learned that the imperfections of the mirrors are critical for the dynamical quantities of the photon gas such as the correlation time, and the effect of this open character of the 'photon box' is discussed in detail in Chapter 3.

1.2 Grand-canonical statistics of the photon gas

The particle number in a gas of bosons fluctuates with a magnitude that is proportional to thermal energy [28]. An everyday example for this phenomenon is the fluctuating number of photons in the emission from a blackbody [29]. Atom number fluctuations were also observed in second-order correlation measurements of ultracold atoms [30–33]. However, the fluctuations completely die-out soon after the boson gas moves over the Bose-Einstein condensation threshold, which happens below a critical temperature or above a critical density [30–32]. Once the atoms accumulate at the ground-state energy of the system, there is no particle exchange with any other state which would induce the fluctuations [33]. In statistical physics, this situation is expressed as the canonical ensemble, which describes a closed system that can not exchange particles with its environment [28, 34]. What happens then, when a Bose-Einstein condensate is allowed to exchange particles with its environment? In this case the statistics of the Bose gas is described by the grand-canonical ensemble; and the particle number fluctuations are expected to be as large as the condensate itself [28, 33]. This large magnitude of the fluctuations has been of particular interest since the original work of Einstein where he predicted the condensation in 1925 [3, 28]. It is remarkable that the large fluctuations originate from the wave nature of the Bose-Einstein condensate in grand-canonical ensemble conditions [3, 33]. In fact, it has been suggested that the connection Einstein makes in his 1925 study, between the particle waves of De Broglie and the large fluctuations of the condensate caused by interference, introduced Schrödinger to De Broglie's work and possibly motivated his further studies [33]. Photon condensates currently emerge as the closest experimental system for an ideal Bose gas in grand-canonical ensemble conditions and the large particle number fluctuations has been observed in second-order, photon-

photon correlation measurements [35]. In Chapter 2, we will describe our experiments where we measure the large fluctuations of the condensate.

In photon condensation experiments, the photons are coupled to photo-excitable dye molecules via absorption and re-emission [10, 17, 26, 36]. This process of photons' and molecular excitations' interconversion constitutes a particle exchange in the sense of a grand-canonical ensemble [16, 35]. Furthermore, the relative size of the particle reservoir with respect to the condensate size can be tuned by adjusting the cavity length, which changes the effective number of molecules that the photons are coupled to [35, 36]. Accordingly, the ensemble conditions of the condensate can be controlled between the canonical statistics where the fluctuations are absent and grand-canonical statistics with large fluctuations [35]. This tuneability of the statistical ensemble conditions is particularly interesting for a study of the fluctuation-dissipation relation, which connects the particle number fluctuations to thermal energy and isothermal compressibility in thermal equilibrium [28, 37]. In photon Bose-Einstein condensation experiments the thermal equilibrium is not disrupted to good approximation as the statistical ensemble conditions are tuned between the canonical and grand-canonical cases. What can we expect then for the validity of the fluctuation-dissipation relation as the condensate is tuned between two limiting cases of very large fluctuations and no fluctuations? Or what can the fluctuation-dissipation relation tell us about the statistical ensemble conditions of a Bose gas? In Chapter 2 we experimentally investigate the fluctuation-dissipation relation in different statistical ensemble conditions.

1.3 Non-Hermitian physics of the photon gas

In physics, the term time-reversal symmetry is used to describe phenomena where the dynamical behavior of the system does not change if the arrow of time is reversed [38]. Consider for example the motion of a harmonic oscillator without friction; it is not possible to determine if the motion is viewed backwards in time. We can classify this example as a closed system, where no dissipative coupling of the system to the environment exist. The dynamics of such systems are mathematically described by Hermitian operators [39]. If we continue from the same example of the harmonic oscillator and introduce an openness, namely friction to the system the motion will be damped. In this case time-reversal symmetry is broken; the dynamical laws evolve in a certain direction and it is possible to determine the arrow of time by observing the dynamical behavior of the system. Dynamics of such open systems are described by non-Hermitian time-evolution operators [39]. Whereas idealized systems that are completely isolated from their environment are useful for a textbook description of physical phenomena, most real systems possess an openness with varying degrees of losses. Therefore, it is not surprising that open systems and non-Hermitian dynamics that describe them are active directions of study across many different fields such as optics, photonics and many-body physics [40–42].

One aspect of the described openness is that the systems move out of equilibrium due to the losses. The state of the system which is characterized in equilibrium is disrupted and the present order might be broken [43]. Consider for example mixing of two solutions with different concentrations,the equilibrium they had before they came into contact with each other is disrupted by the introduced openness once the contact is established. For this reason, dissipation may be seen as a source of disorder. It is therefore interesting that many non-equilibrium processes found in nature have organized structures, with life being a prime example [44]. In fact, both spatial and temporal patterns

may emerge due to such non-equilibrium processes [43–45]. These dissipative, or non-equilibrium structures can be characterized by collective variables (order parameters) that are specific to the system under investigation and are different from the equilibrium order parameters [44]. Consider for example the cases of an equilibrium ferromagnet and a far-from-equilibrium laser [46]. For the ferromagnet, the order of the system is characterized by its magnetization, which can be zero when the spins are disorganized and reaches a maximum value when an ordered state is achieved. For the laser, the emitted photons are mostly out of phase when the atoms are pumped weakly. At a threshold of the pump power, the atomic dipoles start to oscillate in-phase. At this point, the inversion is reached, stimulated emission takes over and consequently the emission of the beam becomes coherent. The magnetization of the ferromagnet and the coherence of the laser are both many-body phenomena that are characterized by collective variables [46]. Therefore, both equilibrium structures and the non-equilibrium patterns that emerge in dissipative systems can be characterized as phases of matter. For non-Hermitian systems in particular, the transition between such dissipative phases often occur at a so called exceptional point where the eigenvalues of the matrix that characterize the system's dynamics coalesce [40, 47–50]

The optical microcavity of the laser, which is externally pumped and has losses through the cavity mirrors is a good example for a system with non-Hermitian dynamics [39]. Similarly for photon Bose-Einstein condensates in dye-filled optical microcavities, which are coupled to a particle reservoir and can be tuned between near-equilibrium and far-from-equilibrium regimes by changing their coupling to the environment, non-Hermitian dynamics are expected. Both of these systems have a broken time-reversal symmetry and collective behavior of photons, but differ in their energy distribution[18] and photon statistics[35]. With these similarities and differences in mind, do certain dissipative structures exist if a system is tuned between a Bose-Einstein condensate and a laser? A non-Hermitian phase transition is expected for a similar case; between a photon laser and a polariton condensate [41, 51]. In Chapter 3 we address this question by studying the non-Hermitian physics of photon Bose-Einstein condensates.

CHAPTER 2

Fluctuation-dissipation relation for a grand-canonical Bose-Einstein condensate

In this chapter we describe our measurements of the density fluctuations and the generalised compressibility of a two-dimensional photon Bose-Einstein condensate confined in a dye microcavity. The photon gas is coupled to a reservoir of molecular excitations, which serves both as a heat bath and a particle reservoir [10]. This leads to grand-canonical statistical behavior with photon number fluctuations of magnitude as large as the average condensate photon number [35]. In thermal equilibrium, such fluctuations are proportionally related to the isothermal compressibility and the thermal energy $k_{\mathrm{B}}T$, as expressed by the fluctuation-dissipation relation.

Fluctuation-dissipation relation has been observed in a variety of systems such as Brownian particles [52], thermal charge fluctuations in electrical resistors [53], soft matter [54] and quantum gases [55],[56]. Despite being intrinsically equilibrium systems, fluctuation-dissipation relations have not been observed in Bose-Einstein condensates so far. In general, the technical noise of the detection methods often makes the fundamental fluctuations in the particle number of the condensate difficult to observe. Recently, atom number fluctuations at the condensation threshold was observed by significantly reducing the technical noise in the ultra-cold atom experiments [57].

For the case of photon condensates, the vanishingly small interactions between photons raise further questions. For instance, consider a gas of photons which is contained in a box with a fixed temperature. In this case where the photons are in equilibrium with the walls of the box, fluctuations of the photon number should occur due to the emission and absorption of photons by the walls. However, the isothermal compressibility is infinitely large for the photon gas because the chemical potential vanishes [58]. This violates the $k_{\mathrm{B}}T$ ratio between the fluctuations and the isothermal compressibility expected from the fluctuation-dissipation relation [59]. It is therefore predicted that fluctuation-dissipation relation does not hold for a photon gas contained in a box [59].

However, a vanishing chemical potential is not an intrinsic property of the photon gas but rather a property of the whole photon box-photon gas system. For instance in a case when the photon box is filled with fluorescent dye molecules, the chemical potential can be non-zero [17]. In photon Bose-Einstein condensates that are confined in a fluorescent dye filled microcavity, a situation similar to the latter case is realized with a two-dimensional photon gas [10]. Further, grand-canonical ensemble conditions are realized in the photon condensate system, with large particle number fluctuations [16, 35]. This makes an experiment observing the fluctuation-dissipation relation for grand-canonical photon

condensates attractive to verify the expected ratio of $k_{\mathrm{B}}T$ between the isothermal compressibility and particle number fluctuations. Earlier theoretical proposals for the study of the fluctuation-dissipation relation to investigate the thermalisation in the dye-microcavity photon condensate system exist [60]. In this Chapter, we describe our measurements where we investigate the validity of fluctuation-dissipation relation for a Bose-Einstein condensed photon gas in the dye-microcavity system.

2.1 Derivation of fluctuation-dissipation relation for the photon gas

2.1.1 Probability distribution

We derive the probability distribution for finding n photons in the condensate by considering different configurations of photons (γ), ground ($\downarrow$) and excited ($\uparrow$) state dye molecules [61], which are subject to the following photochemical reaction.

$$\gamma + \downarrow \rightleftharpoons \uparrow \tag{2.1}$$

The energy cost for the left hand side in eq. (2.1) is $E = n\hbar\Delta$, where $\Delta = \omega_c - \omega_{\mathrm{zpl}}$ denotes the detuning between the condensate frequency ω_c and the frequency associated with the zero-phonon line of the dye molecules ω_{zpl}. The energy mismatch for a configuration of n photons, M_{e} excited and M_{g} ground state dye molecules is illustrated in Figure 2.1.

Let $M = M_{\mathrm{g}} + M_{\mathrm{e}}$ be the total number of dye molecules interacting with the photons. We consider a configuration $r = \{f_1, ..., f_M\}$ of the molecules with n photons, where $f_i = 0$ ($f_i = 1$) if the i-th molecule is in its electronic ground (excited) state. Correspondingly, the total number of excited dye molecules is $M_{\mathrm{e}} = \sum_{i=1}^{M} f_i$, and with the number of condensed photons n, the excitation number X is determined as

$$X = n + \sum_{i=1}^{M} f_i = \text{const.}, \tag{2.2}$$

which in this discussion is considered to be a fixed quantity. The probability for a configuration r

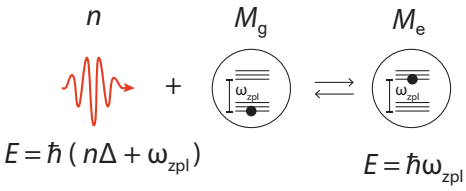

Figure 2.1: Interconversion between photons and dye molecules. A condensed photon carries an energy of $\hbar\omega_c = \hbar(\Delta + \omega_{\mathrm{zpl}})$, while an excited dye molecule M_{e} amounts for a net energy of $\hbar\omega_{\mathrm{zpl}}$. The energy of the ground state molecules M_{g} are set to zero and they do not contribute.

with n photons is then given by the statistical weight

$$\mathcal{P}_{\{f_1,\ldots,f_M\}} = \frac{1}{Z}\exp\left(-\frac{n\hbar\Delta}{k_\mathrm{B}T}\right), \tag{2.3}$$

$$= \frac{1}{Z}\exp\left[-\frac{\hbar\Delta}{k_\mathrm{B}T}\left(X-\sum_{i=1}^{M} f_i\right)\right] \tag{2.4}$$

with the partition function

$$Z = \sum_{f_1=0}^{1}\ldots\sum_{f_N=0}^{1}\exp\left(-\frac{n\hbar\Delta}{k_\mathrm{B}T}\right) \tag{2.5}$$

$$= \sum_{f_1=0}^{1}\ldots\sum_{f_N=0}^{1}\exp\left[-\frac{\hbar\Delta}{k_\mathrm{B}T}\left(X-\sum_{i=1}^{M} f_i\right)\right]. \tag{2.6}$$

Moreover, we have to keep in mind that there are multiple possible configurations with M_e excitations among M molecules. The number of configurations is obtained from a binomial distribution

$$\#_{M_\mathrm{e}} = \begin{pmatrix} M \\ M_\mathrm{e}\end{pmatrix}\left(\frac{1}{2}\right)^{M_\mathrm{e}}\left(\frac{1}{2}\right)^{M-M_\mathrm{e}} \tag{2.7}$$

$$= \frac{M!}{M_\mathrm{e}!\,(M-M_\mathrm{e})!}\frac{1}{2^M} \tag{2.8}$$

$$= \frac{1}{2^M}\frac{M!}{(X-n)!(M-X+n)!} \tag{2.9}$$

By including this degeneracy in eq. (2.4), the probability to find n photons in the condensate mode reads

$$\mathcal{P}_n = \frac{1}{Z}\frac{M!}{(X-n)!(M-X+n)!}\exp\left(-\frac{n\hbar\Delta}{k_\mathrm{B}T}\right), \tag{2.10}$$

and the partition function including the degeneracy for different combinations fom eq. (2.9) is

$$Z = \sum_{n=0}^{X}\frac{M!}{(X-n)!(M-X+n)!}\exp\left(-\frac{n\hbar\Delta}{k_\mathrm{B}T}\right), \tag{2.11}$$

which agrees with earlier results based on a master equation approach [16, 35]. For reasons we will mention later, we can further express both the photon number probability distribution in eq. (2.10) as well as the partition function in eq. (2.11) as a function of the chemical potential $\mu = \mu_\gamma - \hbar\omega_c$ of the photon gas with the cavity cutoff energy $\hbar\omega_c$, instead of the dye cavity detuning Δ. Therefore, we use

$$\exp\left(\frac{\mu}{k_\mathrm{B}T}\right) = \frac{\bar{M}_\mathrm{e}}{\bar{M}_\mathrm{g}}\exp\left(-\frac{\hbar\Delta}{k_\mathrm{B}T}\right) = \frac{X-\bar{n}}{M-X+\bar{n}}\exp\left(-\frac{\hbar\Delta}{k_\mathrm{B}T}\right), \tag{2.12}$$

which is a consequence of the chemical equililbrium between dye molecules and photons, $\mu_\downarrow + \mu_\gamma = \mu_\uparrow$, as explained in Chapter 1. Here, the bars indicate the mean number of photons and molecules in

their electronic ground (excited) state, respectively. The probability distribution becomes

$$\mathcal{P}_n = \frac{1}{Z}\frac{M!}{(X-n)!(M-X+n)!}\left(\frac{M-X+\bar{n}}{X-\bar{n}}\right)^n \exp\left(\frac{n\mu}{k_\mathrm{B}T}\right), \tag{2.13}$$

$$Z = \sum_{n=0}^{X}\frac{M!}{(X-n)!(M-X+n)!}\left(\frac{M-X+\bar{n}}{X-\bar{n}}\right)^n \exp\left(\frac{n\mu}{k_\mathrm{B}T}\right). \tag{2.14}$$

2.1.2 Density fluctuations in the grand-canonical ensemble

In this section we calculate the density fluctuations and obtain the textbook definition of fluctuation-dissipation relations for the grand-canonical ensemble. As a measure of density fluctuations ΔN, mean square deviation of the particle number N is used.

$$(\Delta N)^2 = \bar{N^2} - \bar{N}^2. \tag{2.15}$$

For the grand-canonical ensemble we have the partition function [28]

$$Z = \sum_{i=0}^{N}\exp\left(\frac{\mu N - E_i}{k_B T}\right); \tag{2.16}$$

with the chemical potential μ and energy E. From the partition function we can calculate the average particle number

$$\bar{N} = \frac{k_B T}{Z}\frac{\partial Z}{\partial \mu} \tag{2.17}$$

and the second moment of the particle number

$$\bar{N^2} = \frac{(k_B T)^2}{Z}\frac{\partial^2 Z}{\partial \mu^2}. \tag{2.18}$$

Accordingly the number fluctuations can be written as

$$(\Delta N)^2 = (k_B T)^2\left(\frac{1}{Z}\frac{\partial^2 Z}{\partial \mu^2} - \left(\frac{1}{Z}\frac{\partial Z}{\partial \mu}\right)^2\right). \tag{2.19}$$

Identifying the term in the parantheses with the help of the chain rule as the derivative of $\bar{N}$ with respect to the chemical potential, this gives the fluctuation-dissipation relation in the grand-canonical ensemble [28]

$$(\Delta N)^2 = k_B T\frac{\partial \bar{N}}{\partial \mu}, \tag{2.20}$$

relating $(\Delta N)^2$ to a response function $\frac{\partial \bar{N}}{\partial \mu}$ by thermal energy.

2.1.3 Fluctuation-dissipation relation for the photon gas

The grand-canonical fluctuation-dissipation relation for the Bose-Einstein condensed photon gas can be derived from the above derived partition function eq. (2.14). Following the same steps as in the

previous section we calculate the first- and second-order derivative of the partition function with respect to the chemical potential

$$\frac{\partial Z}{\partial \mu} = \frac{1}{k_B T} \sum_{n=0}^{X} \frac{M!}{(X-n)!(M-X+n)!} \left(\frac{M-X+\bar{n}}{X-\bar{n}}\right)^n n \exp\left(\frac{n\mu}{k_B T}\right), \tag{2.21}$$

$$\frac{\partial^2 Z}{\partial \mu^2} = \left(\frac{1}{k_B T}\right)^2 \sum_{n=0}^{X} \frac{M!}{(X-n)!(M-X+n)!} \left(\frac{M-X+\bar{n}}{X-\bar{n}}\right)^n n^2 \exp\left(\frac{n\mu}{k_B T}\right) \tag{2.22}$$

The sums in eq. 2.22 depend on the average photon number, which prevents us to calculate the average photon number and the second moment of the photon number in the same way as in eqs. 2.17 and 2.18. In the grand-canonical limit $M, X \gg \bar{n}$, the sums do not depend on $\bar{n}$. In addition, the partition function given in eq. (2.14) is valid only if $\left(\frac{M-X+\bar{n}}{X-\bar{n}}\right)^n$ becomes independent of $\bar{n}$, as eq. (2.14) otherwise features a recursion in $\bar{n}$. The issue is circumvented only for $M, X \gg \bar{n}$ (grand-canonical limit). Therefore, at the grand-canonical limit the average photon number and its second moment is written as

$$\frac{d}{d\mu} \ln(Z) = \frac{1}{Z} \frac{\partial Z}{\partial \mu} = \frac{1}{k_B T} \bar{n}, \tag{2.23}$$

$$\frac{1}{Z} \frac{\partial^2 Z}{\partial \mu^2} = \left(\frac{1}{k_B T}\right)^2 \bar{n^2}. \tag{2.24}$$

Accordingly, the first- and second-order derivatives of the partition function with respect to the chemical potential is connected with the mean square deviation of the photon number

$$\left(\frac{1}{k_B T}\right)^2 \left(\bar{n^2} - \bar{n}^2\right) = \frac{1}{Z} \frac{\partial^2 Z}{\partial \mu^2} - \left(\frac{1}{Z} \frac{\partial Z}{\partial \mu}\right)^2. \tag{2.25}$$

In this way the expected fluctuation-dissipation relation for the Bose-Einstein condensed photon gas at the grand-canonical limit is obtained

$$(\Delta n)^2 = k_B T \frac{d\bar{n}}{d\mu}. \tag{2.26}$$

Note that we obtained the same relation with the general definition of the fluctuation-dissipation relation for the grand-canonical ensemble, eq. (2.20) now for the single mode photon condensate. To obtain this result we assumed a reservoir size that is much larger than the condensate photon number, $M, X \gg \bar{n}$, i.e. the grand-canonical limit conditions. While the fluctuation relation describes the system accurately in this limit, for other cases it does not give insight about the system. Grand-canonical conditions are not always realized during the experiments, where the relative reservoir size can be tuned to realize both canonical- and grand-canonical conditions. In the next section we will derive a generalized fluctuation-dissipation relation for photon condensates which is valid for both canonical and grand-canonical ensemble conditions.

2.1.4 Generalized fluctuation-dissipation relation for the photon gas

In the previous section, to obtain the fluctuation-dissipation relation for the grand-canonical ensemble, we used the derivatives of the condensate photon number with respect to the chemical potential. To calculate the generalized fluctuation-dissipation relation we use similar steps as in eqs. 2.22 but take the derivatives of the partition function in eq. (2.11) with respect to the dye-cavity detuning.

$$\frac{\partial Z}{\partial \Delta} = \sum_{n=0}^{X} \frac{M!}{(X-n)!(M-X+n)!} \left(-\frac{n\hbar}{k_{\mathrm{B}}T}\right) \exp\left(-\frac{n\hbar\Delta}{k_{\mathrm{B}}T}\right) \tag{2.27}$$

$$\frac{\partial^2 Z}{\partial \Delta^2} = \sum_{n=0}^{X} \frac{M!}{(X-n)!(M-X+n)!} \left(\frac{n\hbar}{k_{\mathrm{B}}T}\right)^2 \exp\left(-\frac{n\hbar\Delta}{k_{\mathrm{B}}T}\right). \tag{2.28}$$

Similar to the steps in eqs. 2.17 and 2.23 we utilize the logarithmic derivation.

$$\frac{d}{d\Delta}\ln(Z) = \frac{1}{Z}\frac{\partial Z}{\partial \Delta} \tag{2.29}$$

$$= -\frac{1}{Z}\frac{\hbar}{k_{\mathrm{B}}T} \sum_{n=0}^{X} \frac{M!}{(X-n)!(M-X+n)!}\, n \exp\left(-\frac{n\hbar\Delta}{k_{\mathrm{B}}T}\right) \tag{2.30}$$

$$= -\frac{\hbar}{k_{\mathrm{B}}T}\bar{n}. \tag{2.31}$$

The second moment of the photon number is also calculated in analogy with eqs. 2.18 and 2.24.

$$\frac{1}{Z}\frac{\partial^2 Z}{\partial \Delta^2} = \left(\frac{\hbar}{k_B T}\right)^2 \bar{n^2}. \tag{2.32}$$

Accordingly, the mean square deviation of the photon number is written as

$$\left(\frac{\hbar}{k_{\mathrm{B}}T}\right)^2 \left(\bar{n^2} - \bar{n}^2\right) = \frac{1}{Z}\frac{\partial^2 Z}{\partial \Delta^2} - \left(\frac{1}{Z}\frac{\partial Z}{\partial \Delta}\right)^2. \tag{2.33}$$

Plugging eqs. (2.31) and (2.32) to eq. (2.33) gives a generalized fluctuation-dissipation relation for the photon gas:

$$(\Delta n)^2 = -\frac{k_{\mathrm{B}}T}{\hbar}\left(\frac{d\bar{n}}{d\Delta}\right)_X. \tag{2.34}$$

In the generalized relation the chemical potential in the response function is replaced with the detuning. Upon a change of the detuning, the absorption of the molecules are altered. In response, the condensate adjusts its photon number to reach a new equilibrium state. Note that no preassumptions for the reservoir size were applied during the derivation of eq. (2.34). Therefore the obtained generalized fluctuation-dissipation relation is expected to be valid for both canonical- and grand-canonical ensemble conditions, as long as the probability distribution of the photon gas follows the expectation for thermal equilibrium. Experimentally, information about the density fluctuations of the

photon gas is obtained by measuring the second-order correlation function at zero-delay,

$$g^{(2)}(0) = \frac{\overline{n(n-1)}}{\bar{n}^2}. \tag{2.35}$$

It follows that the relation between $g^{(2)}(0)$ and the mean square deviation of the photon number can be written as

$$\left(g^{(2)}(0) - 1\right)\bar{n}^2 + \bar{n} = -\frac{k_B T}{\hbar}\left(\frac{d\bar{n}}{d\Delta}\right)_X. \tag{2.36}$$

This is a generalized fluctuation-dissipation relation for the photon condensate, written as a function of the second-order correlation function at zero-delay. Accordingly, eq. (2.36) can be experimentally verified by simultaneously measuring the second-order correlation function $g^{(2)}(0)$ and the average photon number $\bar{n}$, while varying the dye-cavity detuning Δ at a fixed excitation number X. In the subsequent Section the measurement method is explained in detail.

2.2 Experimental verification of the fluctuation-dissipation relation for the photon gas

2.2.1 Photon correlations behind a beam splitter and on the streak camera

Historically, photon correlation measurements were utilized in landmark experiments measuring the angular diameter of stars by Hanbury Brown and Twiss in 1956 [62] and providing evidence for the indivisibility of photons by Kimble in 1977 [63] and Grangier in 1986 [64]. In the experiments of Hanbury Brown and Twiss, two mirrors separated by a variable distance were employed to collect the light from Sirius, the brightest star of the night sky. The light collected by each mirror was then focused to a separate photomultiplier tube (PMT) and signals coming from each PMT were multiplied. This product gives a direct measurement of intensity correlations. As the distance between the mirrors were increased the correlations drop as theoretically predicted for two distant light sources. By fitting the theoretical correlation versus mirror distance curve to the experimental data, the angular diameters of the stars can be measured. The main benefit of this method is that it is minimally affected by the atmospheric turbulance or irregularities, allowing the measurement of the diameters of more distant stars. Prior to this experiment, Hanbury Brown and Twiss measured the excess fluctuations of a mercury arc light source using the same technique [29]. In this setup, the beam from the arc lamp was wavelength filtered to be nearly monochromatic and then divided into two beams with a half-silvered mirror. Each beam was directed to a separate PMT and the cross-correlation between the signals was recorded. The measured correlaton factor can be written as

$$\alpha = \frac{\langle I_1 I_2 \rangle}{\langle I_1 \rangle \langle I_2 \rangle}, \tag{2.37}$$

where the intensity at each output end of the beam splitter is denoted as I_1 and I_2 and brackets mean an average over multiple measurements. A model of the experiment with classical electromagnetic waves predicts the same intensity value at each output end of the half-silvered mirror, with $I_1 = I_2 = I$ is half of the intensity at the input end of the beam splitter. It follows that the values of $\alpha = \frac{\langle I^2 \rangle}{\langle I \rangle^2}$ will be always equal to or larger than one due to Cauchy-Schwarz inequality. The measured positive

correlations[29] ($\alpha \geq 1$) can be explained classically from the interference of electromagnetic waves from independent emitters [65]. In quantum language, this positive correlation describes closely spaced photons in time and is referred as photon bunching [66, 67].

While Grangier and co-workers' measurement of the second-order correlation function is similar to Hanbury Brown and Twiss, they used single photons in the place of the input beam and observed anti-correlations; a finding which can be explained only with a quantum mechanical description [64]. The result of their experiment can be characterized by the correlation factor

$$\beta = C_{\text{tot}} \frac{C_{1,2}}{C_1 C_2}. \tag{2.38}$$

Here, C_1 and C_2 are the total number of photon counts at each output end of the half-silvered mirror during a certain detection time, $C_{1,2}$ is the number of coincidence counts where photons arrived at both detectors and C_{tot} is the total number of photons that arrive to the input end of the half-silvered mirror and are detected. A quantum mechanical description with single photons predicts values of $\beta = 0$ as a single photon can not be detected twice and $C_{1,2}$ should be zero in this case. Accordingly, the values of $\beta < 1$ in the measurement signals non-classical behavior. Grangier et. al. measured values for β as low as 0.18 ± 0.06 showing an anti-correlation as possible only due to the quantum nature of light [64].

The correlation factor α measured in the experiments of Hanbury Brown and Twiss (eq. (2.37)) and the correlation factor β measured in Grangier and coworkers' experiment (eq. (2.38)) are special cases of the more general second-order photon correlation function [65],

$$g^{(2)}(\tau) = \frac{\langle \hat{n}(t)\hat{n}(t+\tau)\rangle}{\langle \hat{n}(t)\rangle \langle \hat{n}(t+\tau)\rangle}. \tag{2.39}$$

Here, $\hat{n}(t)$ is the number of detected photons at time t and τ is a fixed delay [65]. Values of $g^{(2)}(\tau) < 1$ can only be described quantum mechanically for a steady-state light beam, in contrast to the values of $g^{(2)}(\tau) \geq 1$ where a classical description is also possible. For the case where photon detection is not discrete, the second-order correlation function can be written as a function of the measured intensity $I(t)$ as $g^{(2)}(\tau) = \frac{\langle I(t)I(t+\tau)\rangle}{\langle I(t)\rangle\langle I(t+\tau)\rangle}$.

In addition to the classical and non-classical distinction, $g^{(2)}(\tau)$ characterizes the intensity fluctuation properties of a light beam. In the presence of temporally correlated fluctuations, the inequality $g^{(2)}(\tau) > 1$ holds for time delays of $\tau \ll \tau_c$, where the correlation time τ_c in this case corresponds to the average time required for a relaxation to the steady state value; in other words to lose its correlation. For thermal light sources such as stars or arc lamps, the magnitude of the fluctuations is as large as the mean intensity value, corresponding to $g^{(2)}(0) = 2$. In contrast, values of $g^{(2)}(\tau) = 1$, for any time delay τ describe a light beam where the intensity fluctuations are uncorrelated. In this case the beam is said to be second-order coherent; the laser is the most prominent example of a second-order coherent light source. In this way the value of the second-order correlation function at zero-delay characterizes different states of light.

Whereas the experimental scheme developed by Hanbury Brown and Twiss that measures the photon correlations utilizing a beam splitter and two separate detectors is still widely used, the same information can also be obtained using a single detector [71]. The main advantages of the Hanbury Brown and Twiss setup is to reduce the electronic noise by measuring the cross-correlations of the two

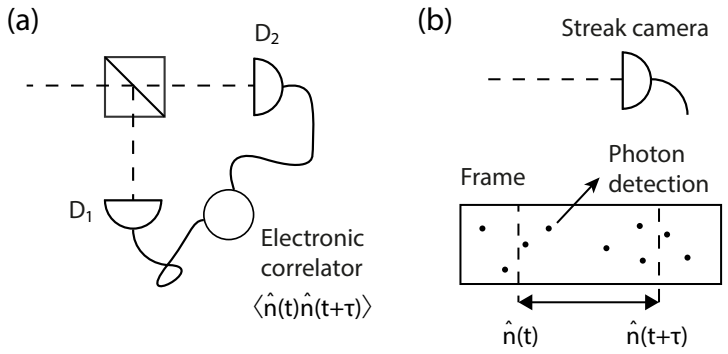

Figure 2.2: Photon correlation measurement schemes for (a) a Hanbury Brown and Twiss setup with a beam splitter and two detectors as used in the above mentioned experiments [29, 62–64] and (b) for a streak camera measurement [68–70]. The vertical axes of the frames can carry spectral or spatial information, depending on the employed setup. In our measurements, the vertical positioning of the photons correspond to spectral dispersion.

detectors [62] and to overcome detector dead times. For a single detector measurement, the detector dead times should be considerably less than the coherence time to ensure the accurate measurement of the photon correlations [71]. During the here-described experiments for the investigation of the fluctuation-dissipation relation for photon condensates, the second-order correlation function is measured with a streak camera by recording the number of detected photons and their arrival times [68–70]. In Figure 2.2, the streak camera measurement scheme is compared with a Hanbury Brown and Twiss setup. In a streak camera measurement, the coincidence counts measured after a beam splitter is replaced by simultaneous photon detections at different pixels of the camera chip. Photons that arrive to the streak camera hit a photocatode and generate electrons. Generated electrons then travel to a fluorescent screen in the presence of an electric field perpendicular to their direction of travel. The amplitude of the electric field is increased rapidly during the detection time, therefore electrons that are generated earlier are deflected more by the field. Consequently, on the deflection axis the spatial information on where the electrons hit the fluorescent screen contains the information of arrival times of the original photons. After the electrons are converted back to photons at the fluorescent screen, they are detected by a 640x480 pixel Charge Coupled Device (CCD) sensor. The 480-pixel axis is reserved for time and the 640-pixel axis can be used to obtain spatial or spectral information as needed. The main advantage of this scheme is the very high time resolution that is achieved; with the streak camera used in our experiments, it is possible to reach a 2 ps time resolution. However, when the photon arrival times are very close on the sensor chip, the determination of the exact position of the photon on the CCD chip may not be possible (see also Ref. [70]). This causes a systematic error in $g^{(2)}(\tau)$ measurements for small τ. The effect of this limitation on our $g^{(2)}(\tau)$ measurements is explained in Appendix A.1. A further advantage of the streak camera measurement scheme is that it is straightforward to count coinciding photon detection events for arbitrary time delays which allows to investigate the evolution of the correlations in time, as well as high-order correlation functions such as $g^{(3)}$ and $g^{(4)}$ [69], while the latter has not been done in this thesis.

In a streak camera measurement, photon detection events are directly visible on the screen, which allows the observation of phenomena such as photon bunching prior to any correlation analysis.

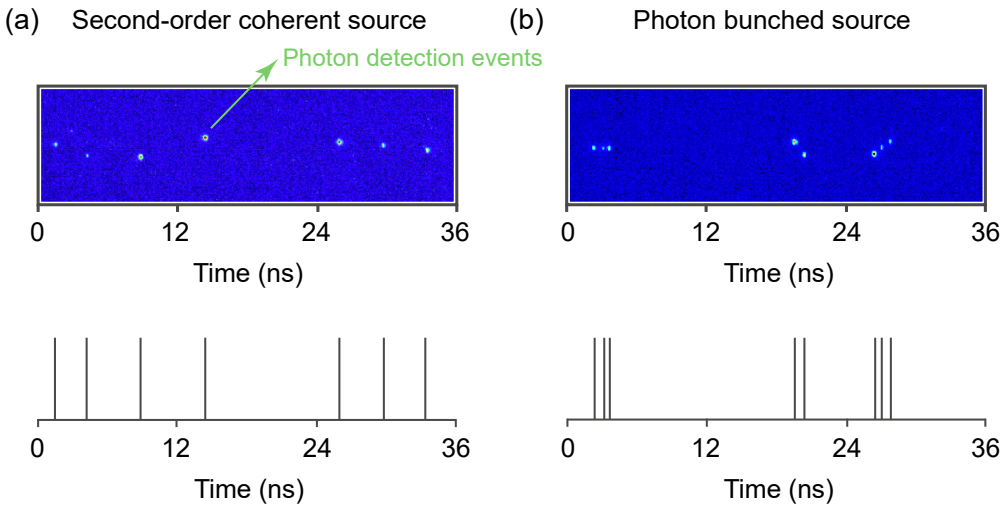

Figure 2.3: Frames recorded by the streak camera showing (a) the random arrival times of photons for second-order coherent light and (b) clumped photons for a photon bunched source (in this case a grand-canonical photon condensate).

Figure 2.3 shows single frames from our measurements of the emission from a coherent and a photon bunched source. In the case of a coherent source such as a laser, photons are randomly distributed in time. Accordingly, the arrival times of photons to the photocathode of the camera is random. In contrast, for the light from a photon bunched source such as a grand-canonical photon condensate, the photons are detected in close time proximity. To calculate the second-order correlation function from these measurements, the arrival times of photons are collected for thousands to millions of frames, from which $g^{(2)}(\tau)$ or higher-order correlation functions can be calculated.

2.2.2 Experimental setup and mode of operation

Dye-filled microcavity

The experimental setup for the thermalisation and Bose-Einstein conensation of photons is similar to those described in detail in earlier works [10, 17, 26, 36]. A sketch of the setup for the current experiment is shown in Figure 2.4. An optical microcavity that consists of two ultra-high reflectivity mirrors with a radius of curvature of $R = 1$m were used in the present experiments. The mirrors are separated with a distance of $d \approx 1.41\mu$m. This spacing is filled with 1 mmol/l rhodamine 6G fluorescent dye dissolved in ethylene glycol. The small mirror spacing ensures a large longitudinal mode spacing which is comparable to the emission width of the dye. In this experimental setting, we observe that only photons from the longitudinal mode number $q = 7$ populate the cavity. The photons are distributed to the two transversal modal degrees of freedom making the system two-dimensional. The fundamental transverse (TEM_{00}) mode of the microcavity sets an upper limit to the optical wavelength and restricts the photon energies to $\hbar\omega_c \approx 2.1$ eV, with minimum cutoff frequency ω_c corresponding to a cutoff wavelength of $\lambda_c \approx 574.9$ nm. To populate the cavity and to compensate for losses such as mirror transmission, the dye-filled microcavity is pumped with a laser beam of 532

nm wavelength, irradiated at an angle near 45° with respect to the optical axis. Two acousto-optic modulators (AOMs) chop the pump laser beam to 500 ns long pulses with a repetition rate of 50 Hz to avoid exciting the molecules to triplet states (see Figure 2.4).

Spectrometer

The microcavity emission comprise the condensate (TEM_{00}) mode and the higher transverse modes. To monitor the cavity during the initial preparation of the condensate, part of the light transmitted from one of the mirrors is imaged on a complementary metal-oxide-semiconductor (CMOS) camera (not shown in the schematic). The rest of the light is directed to a grating and the diffracted light is imaged on a separate CMOS camera which records the spectra. After subtracting the background light and correcting for the wavelength dependent mirror transmission we find that the spectra as a function of wavelength confirm a thermal distribution of photon energies in the cavity (Figure 2.5). As the intensity of the pump beam is increased, a critical photon number in the cavity is reached; a macroscopically populated condensate peak at the position of the cutoff wavelength is observed. At this point the higher energy modes are saturated; upon further increase of the pump intensity, the number of photons in higher order modes which comprise the thermal cloud, remains constant and only the photon number in the ground mode is increased (Figure 2.5). The intensity of the pump beam is therefore used as a tuning parameter for the mean condensate photon number.

Mode filtering

The microcavity emission from the second mirror is directed through a spatial filter and a momentum filter to isolate the condensate mode from the higher order modes. The transmitted light is then sent through a notch filter at 532 nm to remove the scattered light from the pump beam. The filtered light is then focused on a photomultiplier tube (PMT). The signal from the PMT is monitored with an oscilloscope to ensure a temporally averaged, constant cavity population throughout the 500 ns pump pulse. For this purpose the pump pulses are shaped by the AOMs, which are driven by a function generator. After this, a polarizer is placed in the optical path and the signal from the condensate mode is measured with the PMT at two different right angles of the polarizer to measure the degree of polarization of the condensate mode. With the employed microcavity, we observed that approximately 86% of the ground mode emission is in a single polarization mode. The polarizer is set to the angle for the maximum optical signal to lift out the polarization degeneracy.

Photomultiplier detection

The mean electronic PMT signal traces are recorded for each condensate pulse for a pre-determined number of pulses. Simultaneously the optical spectrum is recorded for the same set of pulses using a custom software that synchronises the CMOS camera of the spectrometer with the PMT. After this, the pump power is adjusted to tune the mean condensate photon number in the desired experimental range and the described recording steps are repeated. The PMT signal is then calibrated for the condensate photon number using the measured spectra which relates the photon number in the condensate to the critical photon number in the thermal cloud, $\bar{n_{\mathrm{c}}} = \pi^2/3(k_B T/\hbar\Omega)^2 \approx 81200$. Here, $\Omega \approx 2\pi \cdot 40$ GHz is the trap frequency of the microcavity at the used experimental settings and $T = 300$ K is the room temperature. This calibration measurement is conducted once prior to the main experiment.

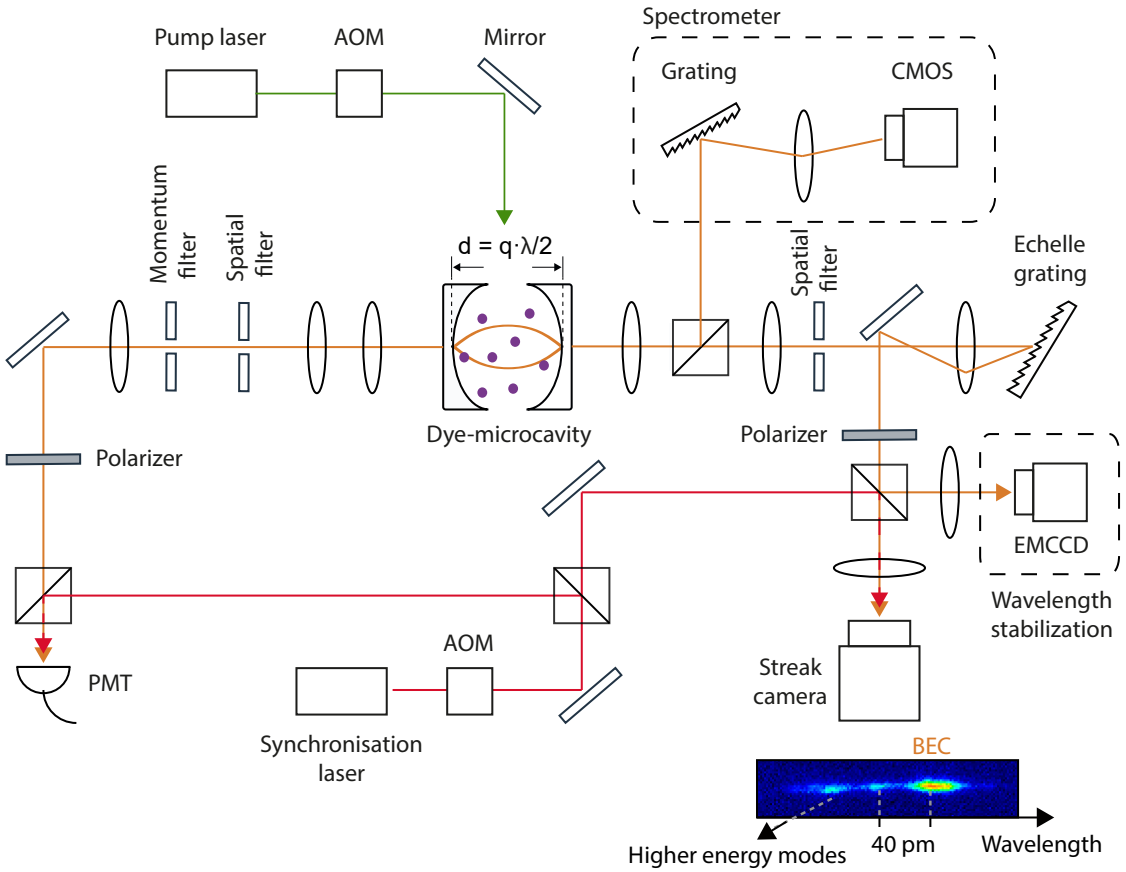

Figure 2.4: Experimental setup. The inset shows an image taken with the streak camera in time-integrated mode, where the condensate mode is spectrally separated from the first excited mode.

To verify the fluctuation-dissipation relations experimentally, the second-order autocorrelation function $g^{(2)}(0)$, the mean photon number and the condensate wavelength must be measured simultaneously (see eq. (2.36)). Therefore, stabilisation measurements for the photon number and the condensate wavelength run continuously during the main experiment. A proportional-integrated (PI) controller algorithm embedded in the PMT readout software tunes the efficiency of the AOMs and keeps the condensate at the desired mean photon number during the measurements. To stabilize the condensate wavelength, part of the cavity emission is directed to an Echelle grating used in Littrow configuration and then imaged on an Electron Multiplying Charge Coupled Device (EMCCD) camera (see Figure 2.4). The high sensitivity of the EMCCD camera is necessary to allow the stabilization of the condensate wavelength with very low levels of light as the rest of the light will be used to collect the photon statistics. A readout software for the EMCCD camera detects the deviations from the desired wavelength and a PI controller tunes the voltage on a piezo crystal that controls the cavity length, d for the wavelength feedback.

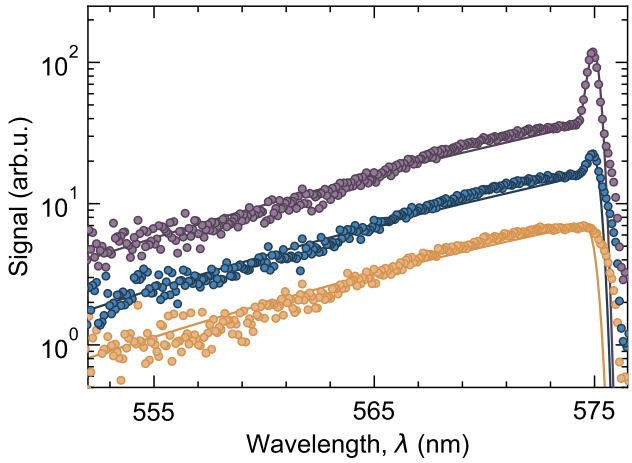

Figure 2.5: Optical spectra of the cavity emission for average condensate photon numbers $\bar{n} \approx 170$ (orange dots), $\bar{n} \approx 1600$ (blue dots) and $\bar{n} \approx 6000$ (purple dots). The solid lines are fits of the Bose-Einstein distribution at 300 K (broadened by the experimental resolution) to the experimental data. The spectra at different $\bar{n}$ are vertically shifted for clarity.

Streak camera detection

The part of the dispersed light that is not used for wavelength stabilization is imaged on the streak camera. Contributions to the correlation signal from the (uncorrelated) thermal cloud photons decreases the magnitude of the measured correlations [35]. Therefore, isolating the condensate photons from the higher transverse mode (thermal cloud) photons is critical for the accurate measurement of photon number correlations. The observed Full Width Half Maximum (FWHM) of the cavity modes on the streak camera of ≈ 20 pm is sufficient to spectrally distinguish the individual transverse cavity modes which are spaced by $\Delta\lambda \approx 40$ pm (see the inset in Figure 2.4). A pulse generator triggers the streak camera at 50 Hz repetition rate and is used as the main trigger of the experiment, switching also the AOMs of the pump laser and the EMCCD. For each condensate pulse, the arrival times of condensate photons on the streak camera, the mean condensate photon number and the condensate wavelength is recorded. Millions of streak camera frames are needed to obtain sufficient statistics for an accurate analysis of the fluctuation-dissipation relation, which corresponds to a measurement time of several days. 50 Hz is the technical limit for the repetition rate of the experiment as it is the maximum frame rate the streak camera can achieve. At this repetition rate, the streak camera from time to time skips a frame, which disrupts the synchronisation of the camera with the rest of the experiment. To solve this timing problem, we used a separate, synchronisation laser which sends optical pulses to the streak camera and the PMT with a comparatively low 1 Hz repetition rate, i.e. one pulse for every fifty streak camera frames (shown with the red beam in Figure 2.4). By counting the streak camera frames between consecutive pulses of this laser, synchronisation of the devices during the long measurement times is ensured.

2.2.3 Measurement of the grand-canonical photon statistics

In the following we describe the measurement of the number fluctuations of the photon condensate using the streak camera scheme described in Sections 2.2.1 and 2.2.2. The maximum allowed detection time of the streak camera of 36 ns was chosen to maximize the collected time-resolved photon statistics. This corresponds to a time resolution of $\Delta t \approx 80$ ps (determined by the pixel density of the CCD chip). This resolution is sufficient for the observation of the typical second-order correlation times of the photon condensates on the order of 2 ns in the experimental parameter range [35, 36].

Figure 2.6(a) shows the recorded photon events from a single streak camera frame for a condensate photon number of $\bar{n} \approx 180$ and ≈ 7900, in the left and right columns, respectively. Due to the low quantum efficiency of the streak camera (approximately 2%) and the small exposure times required for the high time resolution, only a few photons are detected per frame when the condensate photon number is small. For a brighter condensate with a larger photon number, photon detection events are more frequent. For the latter case, the random distribution of photons in time indicates the second-order coherence of the condensate. In contrast, the few photons detected for small condensates are more likely to be observed in close time proximity.

Photons are counted and their observation times recorded from thousands to millions of frames to collect sufficient statistics for the determination of the second-order correlation function. As seen from eq. (2.39), counted photon pairs contribute to the nominator of the second-order correlation function $\langle \hat{n}(t)\hat{n}(t+\tau)\rangle$. The plots in Figure 2.6(b) show the total number of detected photon pairs as well as the detection time of each photon. The time interval between the individual photon detection events is calculated from the observation times of individual photons as $\tau = |t_1 - t_2|$. Note that for small photon numbers (see the left column of 2.6(b)), more pairs are detected when the time interval τ is smaller. In comparison, for the case of the large condensate, the time interval between the photons is uniformly distributed in the detection range of 36 ns, except an artifact at the center diagonal which is caused by the technical limitations of the photon positioning of the streak camera algorithm (see Appendix A).

Figure 2.6(c) shows the $g^{(2)}(\tau)$ functions that are calculated from the recorded images using eq. (2.39). For the case of $\bar{n} \approx 180$ shown in the left column, the value of $g^{(2)}(\tau)$ is larger than 1 for small values of τ. As shown in Figures 2.6(a) and (b), this is a result that quantifies the tendency of photons to bunch together. In particular, the value of the zero-delay second-order correlation function; $g^{(2)}(\tau = 0)$ is a measure of the average amplitude of the number fluctuations as seen in eqs. 2.35 and 2.36. The observed value of $g^{(2)}(0) \approx 2$ means that the average amplitude of the fluctuations is as large as the condensate photon number itself $\bar{n} \approx \bar{\Delta n} \approx 180$. This is an indication for the grand-canonical statistics of the condensate. The measured $g^{(2)}(\tau)$ function for the larger condensate size ($\bar{n} \approx 7900$) is shown in the right column of Figure 2.6(c). In this case, as can be expected from the random distribution of photons in time, the observed correlations are significantly weaker with $g^{(2)}(0) \approx 1$. In Figure 2.6(c), the regions where the correlation signal is modified due to the photon positioning algorithm is shown in gray. The width of this region in time is determined from separate correlation measurements of a laser source (see Appendix A).

Figure 2.7 shows the measured second-order correlation functions for different mean condensate photon numbers. Tuning the condensate size alters both the average amplitude of the fluctuations and the evolution of the correlations in time. The dynamical model for the second-order correlation

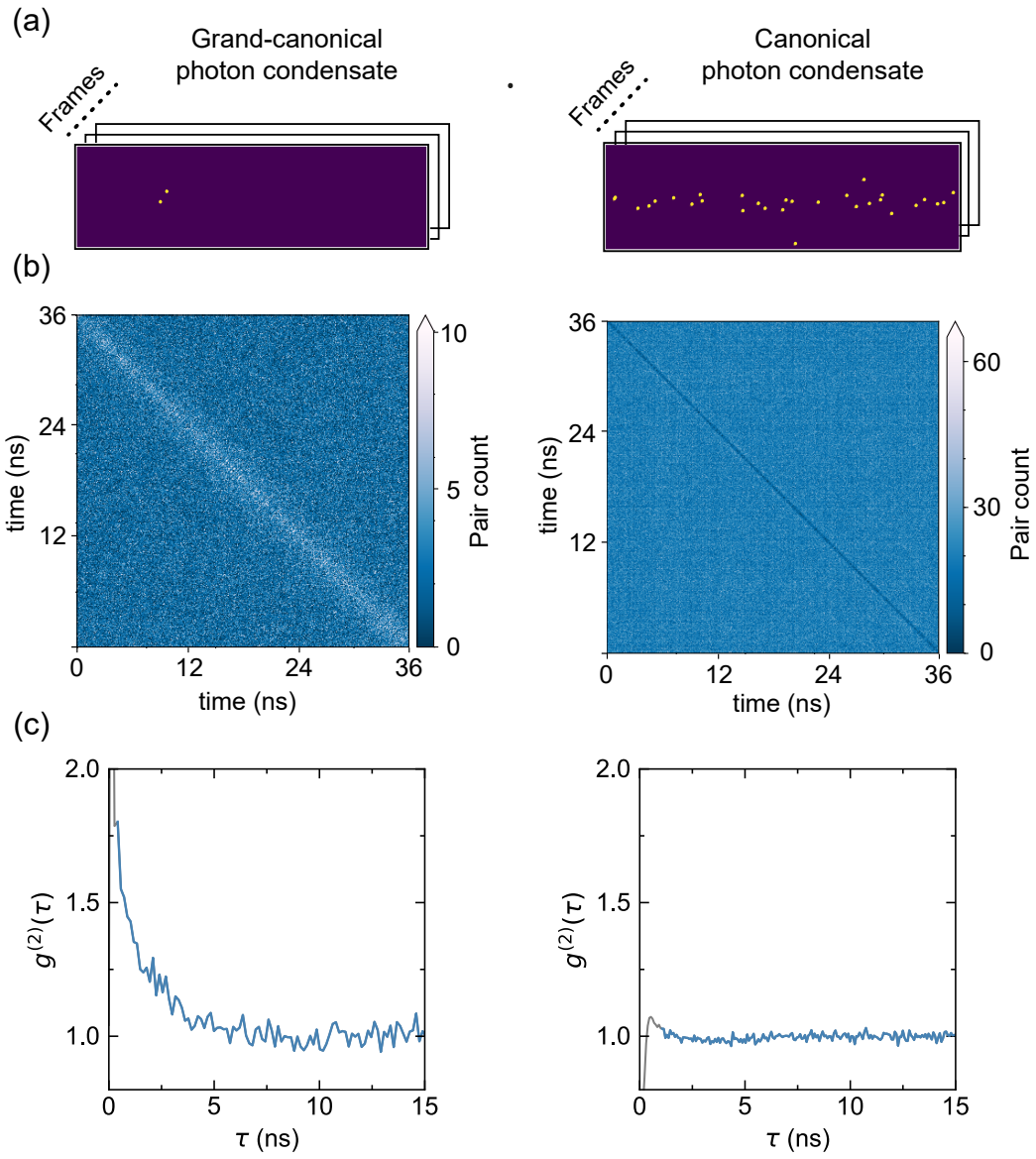

Figure 2.6: Collection of photon statistics for a grand-canonical (left column) and canonical (right column) condensate with photon numbers $\bar{n} \approx 180$ and ≈ 7900, respectively. (a) Arrival times of photons recorded by the streak camera for the grand-canonical and canonical condensates. For the latter, the number of photon counts at each frame is larger as the condensate is brighter at larger $\bar{n}$. Therefore, the total number of frames required for further analysis to acquire a similar amount of statistics is much larger in the case of small condensates. (b) Detection times for the photon pairs, with the horizontal- and vertical-axis showing the detected time of each photon. For small condensates, photons tend to arrive in close time proximities (photon bunching) and the pair count is higher when the detection times are close, whereas for large condensates the time separation of the photons are random and the colormap is flat with no structure. Fewer number of detected photons at zero-time separation for the latter is due to the technical limits of the streak camera see Appendix A). (c) The second-order correlation functions for each case. For small photon numbers the condensate has grand-canonical statistics with $g^{(2)}(0) \approx 2$, whereas for large photon numbers $g^{(2)}(0) \approx 1$ and canonical statistics apply. The gray region is within the pre-determined technical limits of the photon positioning at adjacent pixels and were excluded in the analysis (see Appendix A). Experimental parameters are the longitudinal mode number $q = 7$ and the cutoff wavelength $\lambda_c = 574.86$ nm.

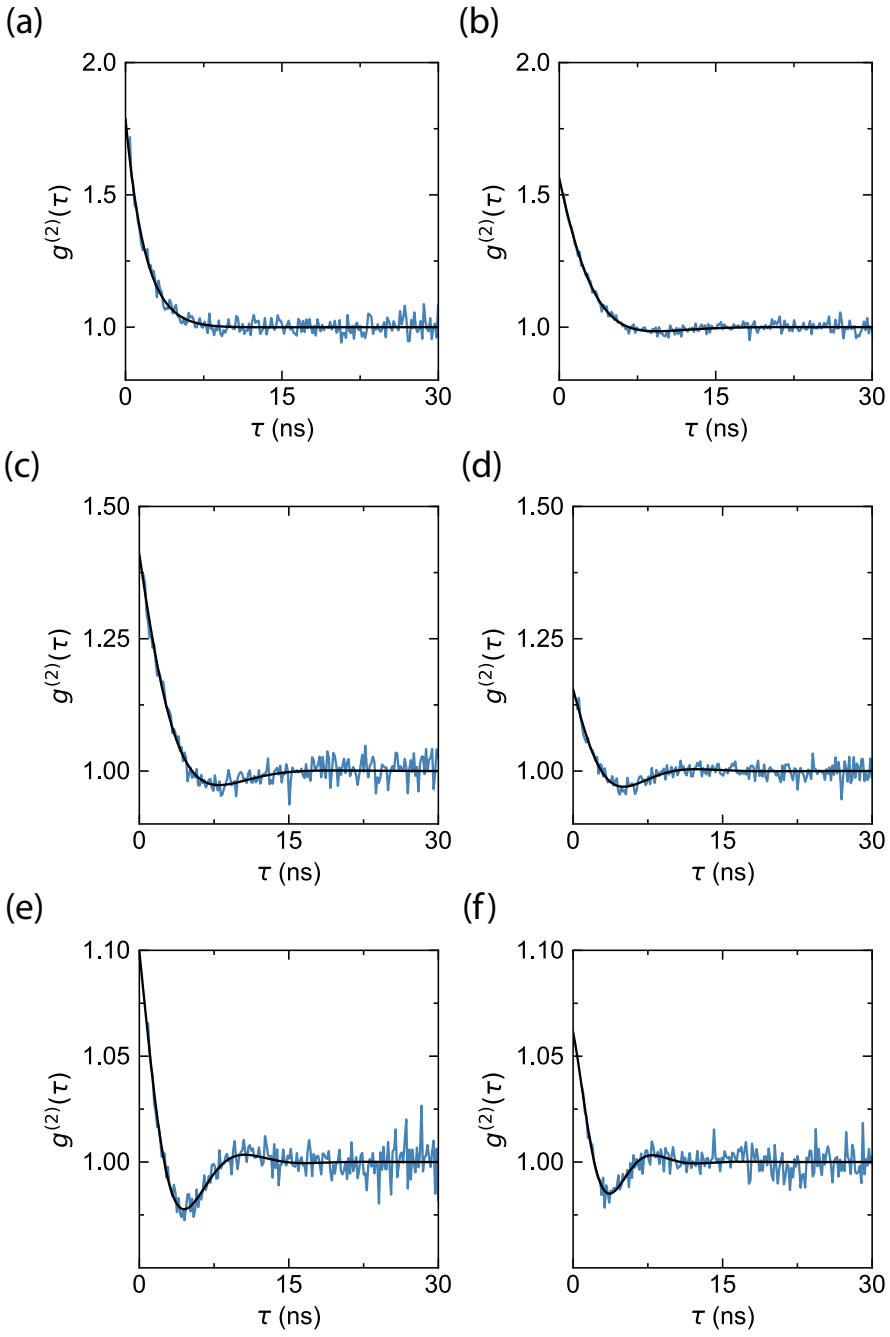

Figure 2.7: Second-order correlation functions measured at different mean condensate photon numbers (blue data) and fits of the dynamical model (black lines) for different mean condensate photon numbers. (a) $\bar{n} \approx 330$ and $g^{(2)}(0) = 1.79(\pm 0.08)$. (b) $\bar{n} \approx 640$ and $g^{(2)}(0) = 1.56(\pm 0.03)$. (c) $\bar{n} \approx 1600$ and $g^{(2)}(0) = 1.41(\pm 0.03)$. (d) $\bar{n} \approx 3300$ and $g^{(2)}(0) = 1.15(\pm 0.01)$. (e) $\bar{n} \approx 5200$ and $g^{(2)}(0) = 1.1(\pm 0.01)$. (f) $\bar{n} \approx 7000$ and $g^{(2)}(0) = 1.06(\pm 0.02)$. Experimental parameters are the longitudinal mode number $q = 7$ and the cutoff wavelength $\lambda_c = 574.86$ nm.

function is given as [72]

$$g^{(2)}(t) = 1 + C_1 e^{\lambda_1 t} + C_2 e^{\lambda_2 t}, \tag{2.40}$$

where C_1, C_2 are constants. The time constants $\lambda_{1,2}$ are related to a natural frequency and the damping rate of the photon number fluctuations. The effect of varying the average photon number on the dynamics of $g^{(2)}(\tau)$ is explained in detail in references [72, 73]. For the study of fluctuation-dissipation relation, we are interested only in the amplitude of the fluctuations. Eq. (2.40) is fitted to the experimental data to determine the value of $g^{(2)}(0)$ (black lines in Figure 2.7). The pre-determined regions of the second-order correlation signal that are altered by the photon positioning algorithm of the streak camera are excluded during the fitting procedure of the $g^{(2)}(\tau)$ functions (see Appendix A). Note that the width of this region in time is small (in the range of 0.45 to 1.4 ns) compared to the time scales shown in Figure 2.7 of 30 ns. In the case of a small condensate with $\bar{n} \approx 330$, the value of the second-order correlation function for small delay times of $\tau \approx 0$ is $g^{(2)}(0) = 1.79(\pm 0.08)$ (Figure 2.7(a)). With increasing τ, the value of $g^{(2)}(\tau)$ decays to one. As the condensate size is increased to $\bar{n} \approx 640$ the value of the second-order correlation function at zero-delay drops to $g^{(2)}(0) \approx 1.56(\pm 0.03)$ (Figure 2.7(b)). The used dynamical model captures the different observed dynamics of the fluctuations in the range of experimental parameters used in this study (black lines in Figure 2.7). As the condensate size is further increased the value of the zero-delay second-order correlation function drops close to unity, with $g^{(2)}(0) = 1.06(\pm 0.02)$ for $\bar{n} \approx 7000$ (Figure 2.7(f)).

Tuning the condensate size influences the statistical exchange of photons with the molecular reservoir, which determines the amplitude of the fluctuations in photon number [16, 17, 35, 36]. For a small condensate size, the effect of spontaneous emission of molecules into the condensate mode on the photon number $n(t)$ plays an important role. Spontaneously emitted photons have no fixed phase relation with the condensate field and the interference of the light field induces fluctuations in the intensity or photon number. In contrast, for larger condensates the coherent feedback due to stimulated emission is more dominant and the fluctuations in the photon number diminish, with $g^{(2)}(0)$ values decreasing as $\bar{n}$ is increased. Figure 2.8 shows the measured $g^{(2)}(0)$ values as a function of the average condensate photon number $\bar{n}$. For very small $\bar{n}$, grand-canonical ensemble conditions are realized with $g^{(2)}(0) \approx 2$. The behavior of the $g^{(2)}(0)$ as a function of the condensate photon number is in good agreement with the numerical calculation of $g^{(2)}(0) = \sum \frac{P_n n(n-1)}{\bar{n}^2}$, with the probability distribution described in eq. (2.10) (solid line in Figure 2.8). An analogous behavior has also been observed in HBT measurements in earlier work, where the maximum value of $g^{(2)}(0) = 2$ could not yet be revealed [35]. This has been achieved for the first time in the present thesis.

Next we investigate the chemical potential of the photon condensate as the statistical ensemble conditions are tuned between the grand-canonical and canonical regimes. The chemical potential, μ is determined from the measured fluctuations in the condensate photon number. As the first step, the measured values of condensate photon number $\bar{n}$ and dye-cavity detuning Δ are plugged in the probability distribution given in eq. (2.14). The detuning, $\Delta = \omega_c - \omega_{zpl}$ is experimentally determined from the condensate wavelength $\lambda_c = 574.86$ nm, which corresponds to $\hbar\Delta/k_B T = -4.57$. The total molecule number is kept fixed at $M = 1.8 \cdot 10^8$ as a global fit parameter and the excited molecule number M_e is left as the only free parameter. Next, a trial value for $g^{(2)}(0)$ is calculated from the probability distribution. M_e is varied to change P_n until the trial value converges to the experimental $g^{(2)}(0)$ value. After the converged probability distribution is obtained, the chemical potential is calculated with $\mu/k_B T = \ln(z)$, where the fugacity z is calculated with $z = (M_e/M) \cdot e^{\hbar\Delta/k_B T}$.

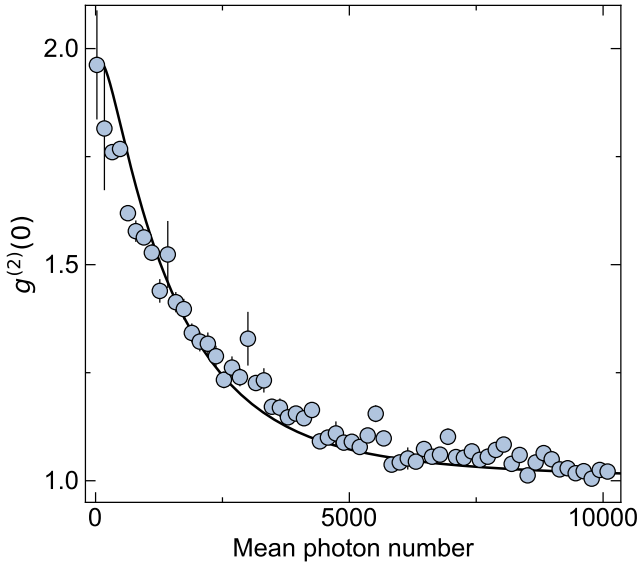

Figure 2.8: Zero-time second-order correlations $g^{(2)}(0)$, as a function of the mean condensate photon number $\bar{n}$. The solid line indicates the numerical solution of the theoretical model given in eq. (2.11) for a molecule number of $M = 1.8 \cdot 10^8$. Error bars are calculated from the uncertainties of the fit parameters. Experimental parameters are $\lambda_c = 574.86$ nm for the cavity cutoff wavelength and $q = 7$ for the longitudinal mode number.

The determined chemical potential values are shown as a function of the mean condensate photon number in Figure 2.9. For smaller condensates, where the value of the zero-delay second-order correlation function is larger than unity, we observe a non-vanishing chemical potential. In general, for a Bose-Einstein condensate realized in canonical statistical ensemble conditions the chemical potential becomes non-vanishing only near the condensation threshold. In contrast, a non-vanishing chemical potential is observed here deep in the Bose-Einstein condensed phase. This is a consequence of the grand-canonical statistical conditions allowed with the coupling of the condensate with a molecular reservoir. For larger mean condensate photon numbers where canonical statistical ensemble conditions are realized, the value of the chemical potential approaches zero (Figure 2.9). By changing the mean condensate photon number, the system is tuned between a case where the isothermal compressibility is infinitely large, along with a vanishing chemical potential and a case with a non-vanishing chemical potential where a scaling of $k_{\mathrm{B}}T$ with the isothermal compressibility is expected following the fluctuation-dissipation relation given in eq. (2.26).

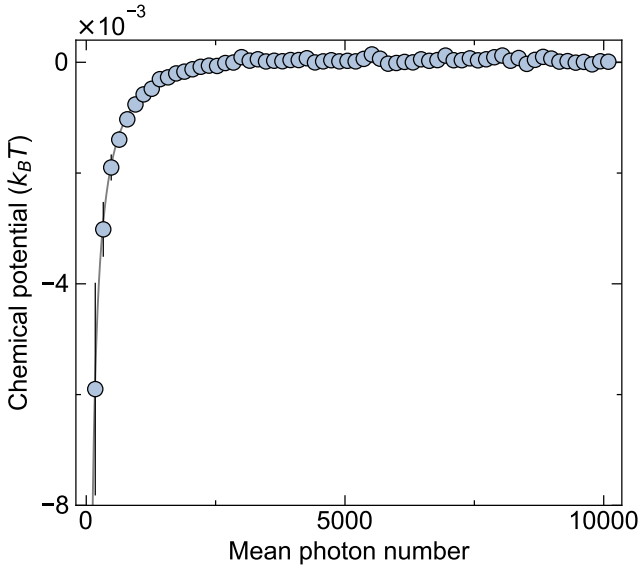

Figure 2.9: Chemical potential as determined from the fugacity $z = e^{\mu/k_{\mathrm{B}}T}$, plotted as a function of the mean condensate photon number $\bar{n}$. The solid line indicates the numerical solution of the theoretical model given in eq. (2.14) for a molecule number of $M = 1.8 \cdot 10^8$. Error bars are calculated from the error in the $g^{(2)}(0)$ measurements, which are used to obtain the fugacity. Experimental parameters are $\lambda_c = 574.86$ nm for the cavity cutoff wavelength and $q = 7$ for the longitudinal mode number.

2.2.4 Measurement of a generalized fluctuation-dissipation relation

In this section, we describe experiments which reveal a ratio of $k_{\mathrm{B}}T$ between the number fluctuations and a generalized compressibility, namely the generalized fluctuation-dissipation relation given in Section 2.1.4. To check the validity of eq. (2.36), we need to measure the average amplitude of the photon number fluctuations quantified by the zero-delay second-order correlation function, $g^{(2)}(0)$ and the generalized response, $(d\bar{n}/d\Delta)_{X,T,V}$. For this purpose, we recorded the zero-delay second-order correlation data along with the mean condensate photon number and the dye-cavity detuning as we continuously tuned the pump intensity and the cavity length. In Sections 2.2.1 and 2.2.3 the measurement of the $g^{(2)}(0)$ values is explained in detail. In addition, the measurement schemes for the mean photon number, $\bar{n}$ and the condensate wavelength, λ_c are described in Section 2.2.2. From the condensate wavelength and the zero phonon line frequency of the dye, the dye-cavity detuning, $\Delta = \omega_{\mathrm{c}} - \omega_{\mathrm{zpl}}$ is calculated.

Note that the excitation number, $X = \bar{M}_e + \bar{n}$ should be fixed along with the temperature and the volume of the photon gas to measure the generalized response of the condensate. The temperature of the dye medium is fixed at 300 K and the effective volume is determined by the mirror curvature with $V = 1/\Omega^2$ (s^2), where $\Omega \approx 2\pi \cdot 40$ GHz is the trapping frequency of the optical microcavity. However, the excitation number X is highly sensitive to the changes in the intensity of the pump beam and the dye-cavity detuning. To determine and fix the excitation number, it is necessary to count the number of excited molecules, M_e which is not directly accessible in our experiment. Therefore, X is determined from the recorded mean photon numbers. To achieve this, theoretically calculated mean photon numbers, $\bar{n} = \sum P_n \cdot n$ were fitted to the measured mean photon numbers for all of

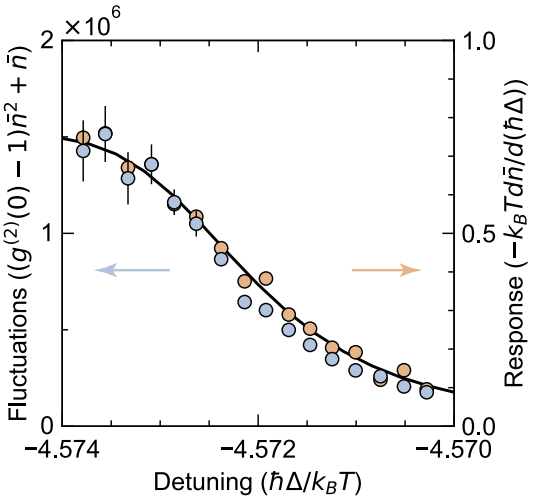

Figure 2.10: Generalized fluctuation-dissipation relation for a Bose-Einstein condensate of photons. The left and right vertical axes represent the left- and right-hand side of eq. (2.36), respectively. The expected scaling of $k_{\mathrm{B}}T$ between the number fluctuations and generalized compressibility is confirmed deep in the grand-canonical and canonical regimes for $\hbar\Delta/k_BT = -4.570$, and -4.574, respectively. For the former case, the effective reservoir size is a factor of 6 larger than the mean photon number squared. In contrast, the reservoir size is a factor of 25 smaller than the mean photon number squared for the latter case. The excitation number is $X = 1.535 \cdot 10^6$, the molecule number $M = 1.5 \cdot 10^8$, the longitudinal mode number $q = 7$ and the temperature $T = 300$ K. The solid line shows eq. (2.36) for the given parameters.

the recorded data points using the excitation number as a fit parameter. Here, P_n is the probability distribution given in eq. (2.10). The measured values of the dye-cavity detuning for each data point, the room temperature $T = 300K$ and the fixed total molecule number $M = 1.5 \cdot 10^8$ were used in eq. (2.10) and X was the only fit parameter. In this way, we obtained a matrix with the corresponding data points for $g^{(2)}(0)$, $\bar{n}$, Δ and X. Values of $g^{(2)}(0)$, $\bar{n}$ and Δ for a fixed excitation number of $X = 1.535 \cdot 10^6$ were selected from this data matrix by finding the nearest points to this pre-set value. This chosen value of X correspond to the region with the most data points in the data matrix. Note that the determination of X is only required to guarantee the condition of constant X and does not enter the parameters plotted, which are purely experimental.

The left- and right-hand side of eq. (2.36) were calculated from the obtained data points for fixed X, T and V values to determine the fluctuations and response of the condensate, respectively. The results are shown in Figure 2.10. We observe a good agreement of the measured values for the two sides of eq. (2.36) across the investigated detuning range. The obtained experimental data follows the theoretically expected scaling of $k_{\mathrm{B}}T$ between the fluctuations and the generalized compressibility. The black line in Figure 2.10 is the theoretical calculation of eq. (2.36) for the used experimental parameters. Notably, the photon condensate is tuned between the canonical and grand-canonical statistical ensemble conditions in the investigated dye-cavity detuning range. The dye-cavity detuning is a tuning parameter for the statistical ensemble conditions of the photon gas since it is connected with the Einstein coefficients for absorption, B_{abs} and emission, B_{em} with the Kennard-Stepanov relation, $B_{\mathrm{em}}/B_{\mathrm{abs}} = \exp(-\hbar\Delta/k_BT)$. By adjusting the condensate wavelength closer to the

zero-phonon line and hence decreasing the absolute value of the dye-cavity detuning, the ratio of the Einstein coefficients is changed in favor of B_{abs}. This increase of the Einstein coefficient for absorption increases the number of excited molecules and leads to a larger size of the effective particle reservoir $M_{\mathrm{eff}} = M/[2 + 2\cosh(\hbar\Delta/k_B T)]$ [35, 36]. Note that while the dye-cavity detuning and hence the number of excited molecules is adjusted, the excitation number $X = \bar{M}_e + \bar{n}$ is kept constant. An increase of the excited molecule number is accompanied with a decrease of the mean condensate photon number. Therefore, even a slight change in the dye-cavity detuning modifies the statistical ensemble conditions greatly. In our experiments, the total number of molecules was kept constant and the detuning was varied between $\hbar\Delta/k_B T = -4.570$, and -4.574. Grand-canonical statistical ensemble conditions are realized when the effective particle reservoir is quadratically larger than the condensate photon number [35]. For the smallest absolute value of the detuning in our experiments ($\hbar\Delta/k_B T = -4.570$), the effective particle reservoir is a factor of six larger than the mean photon number squared. In this limit, the grand-canonical conditions are fulfilled. In contrast, for $\hbar\Delta/k_B T = -4.574$ the effective reservoir size is more than an order of magnitude smaller than the mean photon number squared and the condensate is in the canonical regime. Additional data where the excitation number of the photon condensate is fixed to $X = 1.536 \cdot 10^6$ and $X = 1.537 \cdot 10^6$ is shown in Figure 2.11.

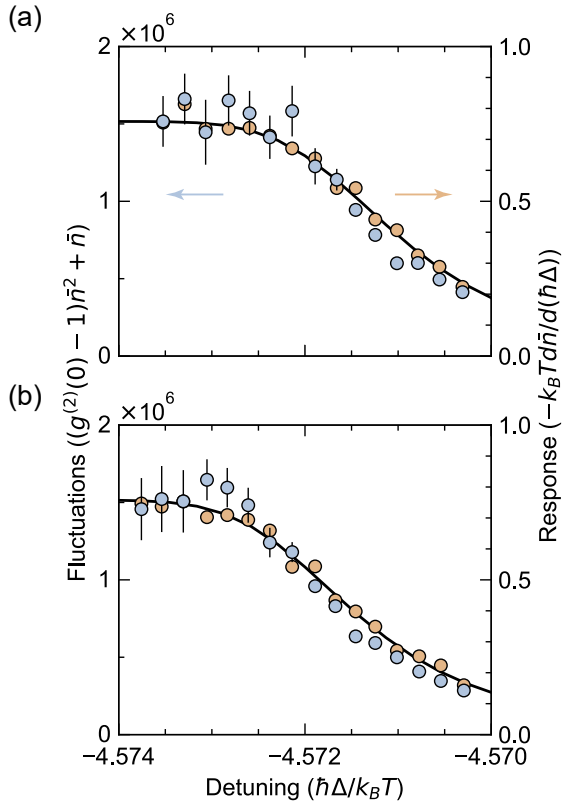

Figure 2.11: Generalized fluctuation-dissipation relation for a Bose-Einstein condensate of photons for the case where the excitation number is fixed to (a) $X = 1.537 \cdot 10^6$ and (b) $X = 1.536 \cdot 10^6$. The molecule number is $M = 1.5 \cdot 10^8$ and the longitudinal mode number $q = 7$. The solid line shows eq. (2.36) for the given parameters.

2.2.5 Determination of the thermodynamic compressibility

In this section we describe the results of our experiments investigating the validity of the textbook definition of the fluctuation-dissipation relation for an ideal gas in grand-canonical ensemble conditions. Here, a ratio of $k_\mathrm{B}T$ between the density fluctuations, $(\Delta n)^2$ and the response function $(d\bar{n}/d\mu)_{T,V}$ is expected, where μ is the chemical potential. For a photon gas coupled to a dye-microcavity, both canonical and grand-canonical statistical ensemble conditions can be realized depending on the size of the particle reservoir which is controlled by the dye-cavity detuning in the experiments. We expect that for a small absolute value of the dye-cavity detuning, conditions for an ideal gas in the grand-canonical ensemble is realized and the textbook definition for the fluctuation-dissipation relation given in eqs. (2.20) and (2.26) hold in the system. In contrast, when the dye-cavity detuning is adjusted for a smaller effective particle reservoir size, the system is expected to deviate from this scenario as it is tuned toward canonical ensemble conditions. See Sections 2.1.2 and 2.1.3.

The difference between the conventional textbook definition of the fluctuation-dissipation relation (eq. (2.26)) and the generalized version which holds regardless of the statistical ensemble conditions (eq. (2.36)) is only in the response function, $(d\bar{n}/d\mu)_{X,T,V}$ where the chemical potential, μ is

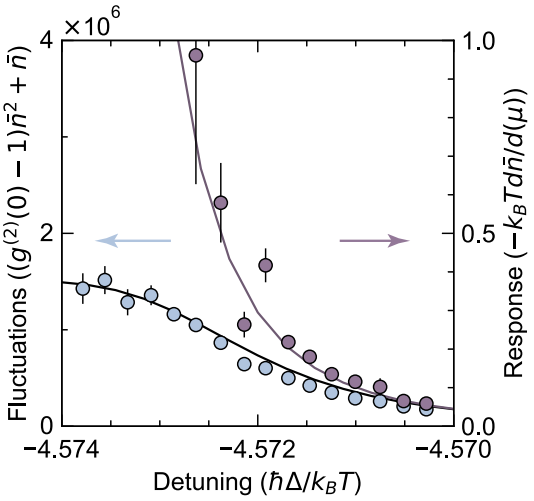

Figure 2.12: Thermodynamic fluctuation-dissipation relation for a Bose-Einstein condensate of photons. In contrast with the generalized relation which holds regardless the statistical ensemble conditions, the textbook definition is expected to hold only in the true grand-canonical ensemble conditions. The expected scaling of $k_{\mathrm{B}}T$ between the number fluctuations and isothermal compressibility holds only deep in the grand-canonical regime, close to dye-cavity detuning values of $\hbar\Delta/k_BT = -4.570$. For larger absolute values of the dye-cavity detuning, the response function (purple dots) deviate from the observed fluctuations (blue dots) and diverge as the condensate is moved deep into the canonical regime close to dye-cavity detuning values of $\hbar\Delta/k_BT = -4.574$. The excitation number is $X = 1.535 \cdot 10^6$, the molecule number $M = 1.5 \cdot 10^8$ and the longitudinal mode number $q = 7$. The solid lines are calculated from the probability distribution for the given experimental parameters (eq. (2.26)).

replaced by the dye-cavity detuning in the generalized version. Data from the same measurement run is analysed to check the validity of both equations. As described in the previous section the zero-delay second-order correlation data, the mean condensate photon number and the dye-cavity detuning are recorded simultaneously, while the latter two are slightly tuned. In addition, the excitation number, X is determined from the mean photon numbers, $\bar{n}$ for each data point and kept fixed at a pre-set value by post-selecting the data points corresponding to this value from the data pool (see also Section 2.2.4). In addition, the chemical potentials were determined from the measured fluctuations in the condensate photon number as described in Section 2.2.3.

Figure 2.12 shows the measured fluctuations and the response function as the condensate is tuned between the canonical and grand-canonical statistical regimes with the data from the same measurement run as shown in Figure 2.10. We observe that for small absolute values of the dye-cavity detuning close to $\hbar\Delta/k_BT = -4.570$, the fluctuation-dissipation relation hold with a scaling of $k_{\mathrm{B}}T$ between the fluctuations and the response function. At this dye-cavity detuning value, the reservoir size is a factor of 6 larger than the mean photon number squared and the system is deep in the grand-canonical regime with $M_{\mathrm{eff}} \gg \bar{n}^2$. Therefore, conditions where the textbook definiton of the fluctuation-dissipation relation is derived, namely an ideal Bose gas in the grand-canonical ensemble is realized in the experiments. In addition, a non-vanishing chemical potential, $\mu/k_{\mathrm{B}}T = -2 \cdot 10^{-3}(\pm 6 \cdot 10^{-6})$ is observed in this limit. In contrast, when the detuning value is tuned

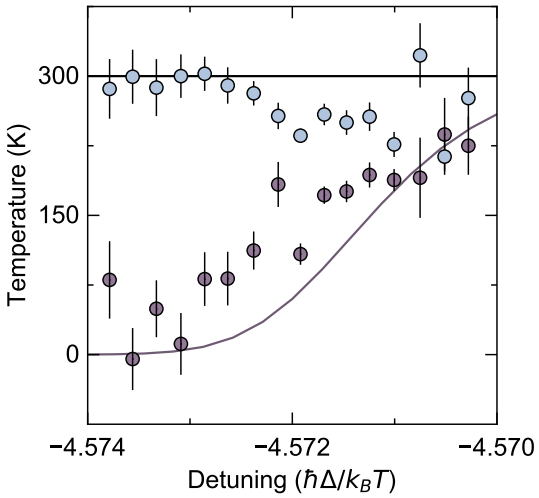

Figure 2.13: Temperatures extracted from the textbook and generalized versions of the fluctuation-dissipation relation as a function of the dye-cavity detuning shown in purple and blue dots, respectively. In the grand-canonical ensemble conditions with the dye-cavity detuning values close to $\hbar\Delta/k_BT = -4.570$, the temperatures extracted from both versions approach the temperature of the dye solution, 300 K. For larger absolute values of the dye-cavity detuning, the temperature extracted from the textbook fluctuation-dissipation relation (purple dots) deviate from this value as the condensate is moved deep into the canonical regime. The excitation number $X = 1.535 \cdot 10^6$, the molecule number $M = 1.5 \cdot 10^8$ and the longitudinal mode number $q = 7$. The solid lines are calculated using the probability distribution for the given experimental parameters.

to $\hbar\Delta/k_BT = -4.574$ while keeping X, T and V constant, we observe that the response function strongly deviate from the scaling of $k_\mathrm{B}T$ predicted by the grand-canonical fluctuation-dissipation relation. The reason of this deviation is the changing statistical ensemble conditions of the photon gas. At he detuning value of $\hbar\Delta/k_BT = -4.574$, the condensate is deep in the canonical statistical limit, with $M_\mathrm{eff} < \bar{n}^2/25$. In this limit, the value of the chemical potential approaches to zero within the experimental sensitivity, $\mu/k_\mathrm{B}T = -2 \cdot 10^{-5}(\pm 2 \cdot 10^{-5})$. With a vanishing chemical potential, isothermal compressibility becomes infinitely large for the photon gas and the textbook definition of the fluctuation-dissipation relation is not valid in this limit [58, 59]. The deviation from the fluctuation-dissipation relation is also predicted from a calculation using the probability distribution given in eq. (2.10), which is valid both in canonical and grand-canonical statistical ensemble limits.

Since the fluctuation-dissipation relation predicts a scaling with the thermal energy $k_\mathrm{B}T$, the experimental investigation of these relations allows the determination of the temperature of the system associated with the fluctuations. The temperature is obtained by $T = \frac{\hbar}{k_\mathrm{B}} \frac{\bar{n}^2(g^{(2)}(0)-1)}{(d\bar{n}/d\mu)_{X,T,V}}$. Similarly, to obtain the temperature for the generalized fluctuation-dissipation relation, the chemical potential is replaced by the dye-cavity detuning in the given formula. Figure 2.13 shows the temperatures extracted from both the generalized and the textbook fluctuation-dissipation relation as a function of the dye-cavity detuning. For a grand-canonical condensate at smaller absolute values of the dye-cavity detuning, the extracted temperature approaches 300 K; the temperature of the dye solution. However, as the statistical ensemble conditions of the condensate is tuned towards a canonical ensemble the temperature extracted from the textbook fluctuation-dissipation relation deviate from this value. As

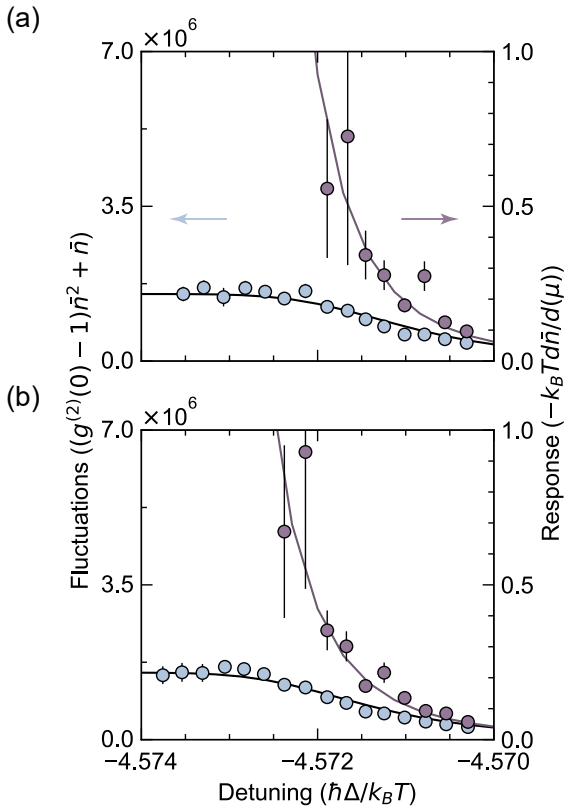

Figure 2.14: Fluctuation-dissipation relation for a Bose-Einstein condensate of photons for the case where the excitation number is fixed to (a) $X = 1.537 \cdot 10^6$ and (b) $X = 1.536 \cdot 10^6$. The data is from the same measurement run as shown in Figure 2.11. The molecule number $M = 1.5 \cdot 10^8$ and the longitudinal mode number $q = 7$. The solid lines show eq. (2.26) for the given parameters.

seen in Figure 2.13, as the absolute value of the detuning is increased the extracted temperature drops towards zero for the textbook case. This deviation is a manifestation of the diminishing fluctuations of the photon gas. For an ideal gas in grand-canonical ensemble conditions, the particle number fluctuations are present as long as the temperature is above absolute zero (see eq. (2.26)). The temperature extracted from the fluctuation-dissipation relation is altered when the statistical ensemble conditions are changed towards the canonical ensemble regime, even if other thermodynamic properties of the gas are the same. The temperature extracted from the generalized version of the fluctuation-dissipation relation do not show this variation towards zero as the absolute value of the dye-cavity detuning is increased (Figure 2.13). As explained in the previous Section, the generalized fluctuation-dissipation relation is valid independent of the statistical ensemble conditions of the photon gas.

Additional data for the textbook definition of the fluctuation-dissipation relation, where the excitation number of the photon condensate is fixed to $X = 1.536 \cdot 10^6$ and $X = 1.537 \cdot 10^6$ is shown in Figure 2.14.

2.3 Discussion

In this chapter, we experimentally showed that the fluctuation-dissipation relation holds for a Bose-Einstein condensate of photons under grand-canonical ensemble conditions. As the condensate is tuned away from the grand-canonical regime towards the canonical ensemble conditions, its behavior deviates away from the expected ratio of $k_{\mathrm{B}}T$ between the fluctuations and response. As the canonical limit is reached, the fluctuations of the photon number diminish and the chemical potential vanishes. We derived and experimentally verified a generalized version of the fluctuation-dissipation relation where the chemical potential is replaced by the dye-cavity detuning. The generalized version of the relation holds independently of the statistical ensemble conditions, i.e. both in canonical and grand-canonical regimes. The non-vanishing chemical potential of the photon gas in our system is not related to a net diffusion of particles in space or inter-particle interactions, but to the excitation level of the medium. The dye-cavity detuning adjusts the excitation level of the medium. The excitation level of the medium in turn adjusts the probability distribution and hence the photon number in the condensate. In this sense, it is intuitive that the dye-cavity detuning replaces the chemical potential in the generalized version of the fluctuation-dissipation relation. Our results further demonstrate that, contrary to the usual understanding [59], the fluctuation-dissipation relation holds for a photon gas if environmental conditions are realized where its chemical potential does not vanish.

The dissipation we observe in this study with the response function $d\bar{n}/d\mu$ is an equilibration mechanism that is driven by fluctuations. This understanding of the phenomenon of dissipation is the essence of fluctuation-dissipation relations. Thermal energy causes fluctuations which drive the system to probe different probable states. In this process the system moves towards equilibrium, the most probable state. In this sense, dissipation is ever-present also in closed systems. For instance, the diffusion constant in a liquid solution is not zero as long as the temperature is above zero. However, diffusion is only observable as a net flow of particles when there is an external perturbation which causes a concentration gradient [52]. In our system, the Bose-Einstein condensate adjusts its particle number when the excitation level of the dye medium is externally tuned.

CHAPTER 3

Open-system dynamics of the fluctuations in a Bose-Einstein condensate

In this chapter we will investigate how a photon flow from the molecules to the condensate, and from the condensate to outside of the cavity affects the dynamics of the photon number fluctuations. As described in Chapter 2, during our investigation of the (time-independent) fluctuation-dissipation relation, we observed no significant effect of this residual photon flow to the average amplitude of the fluctuations. A deviation from thermal equilibrium was observed however, in the temporal evolution of the second-order correlation function, which deviates from a pure exponential decay as shown in for example Figure 2.7. Such oscillatory dynamics in open dye microcavity systems have been recently studied [73, 74] and will be explained in this chapter in detail. In this chapter, we further demonstrate a non-Hermitian phase transition to a novel dissipative phase in a photon Bose-Einstein condensate coupled to the environment [72]. New phases of matter which arise due to the interaction of a system with its environment has recently been observed in a variety of research fields such as optics, materials science and biophysics [40, 45, 73, 75–78]. Also in quantum many-body physics, such driven-dissipative phases are currently actively studied [41, 79–82]. This openness of the system to its surroundings can be induced by for example a gain and a loss channel. However, for the case of ultracold atomic quantum gases, an openness to the environment usually involves a process of heating up the system, making it a challenge to study any quantum dissipative phases that would emerge [83, 84].

In contrast to experiments on cold atoms where the condensate is isolated from the environment, photonic and semiconductor hybrid platforms are open systems where the light that leak out of the mirrors is compensated with a pump beam [85]. The driving and loss in this open setting move the systems away from thermal equilibrium [86–88]. Nevertheless, phenomena such as condensation [8, 89], superfluidity [90] and quantized vortices [91] have been observed even in the presence of dissipation. Theoretically, while closed physical systems are described by Hermitian operators with real eigenvalues, a dissipative coupling to the environment is described by a non-Hermitian operator, for which the eigenvalues are complex. For such non-Hermitian systems, so called exceptional points, where the eigenvalues and the corresponding eigenmodes coalesce, mark dissipative phase transitions [41, 47, 48, 92]. Recent theory works have proposed a first-order phase transition at an exceptional point between a photon laser and a polariton condensate, and also pointed out that at exceptional points critical fluctuations can occur in these systems [51, 81]. In our experiments

described in this chapter, an exceptional point in the Bose-Einstein condensed photon gas is revealed by monitoring a well-defined transition from the oscillatory behavior to a biexponential decay of the second-order coherence at an exceptional point [72]. The phases exist due to the coupling of condensate photons to a reservoir of dye molecules along with time reversal symmetry breaking from pumping and loss. Despite the driven-dissipative character, on both sides of the phase transition, the observed spectrum displays a condensate peak as well as a thermal cloud, in good agreement with the predictions of equilibrium statistics. This transition occurs within the regime of spontaneously broken time-reversal symmetry, which is common to both lasing and condensation [93, 94]. However, while the first, oscillatory phase at high losses is expected to cross over to the regime of lasing, the second, biexponential phase is separated from these observed phenomena by a dissipative phase transition.

3.1 Rate equation description of the open-system dynamics of the photon gas

The particle flow in the dye-microcavity system, which is visualised in Figure 3.1 is described with the following coupled rate equations:

$$\frac{dn}{dt} = [B_{em}M_{\mathrm{e}}(n+1) - B_{abs}M_{\mathrm{g}}n] - \kappa n, \tag{3.1}$$

$$\frac{dM_{\mathrm{e}}}{dt} = -[B_{em}M_{\mathrm{e}}(n+1) - B_{abs}M_{\mathrm{g}}n] + R_{\mathrm{p}}M_{\mathrm{g}}. \tag{3.2}$$

Here, n is the time-dependent photon number in the condensate at a given instant, $n = \bar{n} + \Delta n$, where $\bar{n}$ is the mean photon number and Δn is a deviation from the mean value. Note that here the mean values such as $\bar{n}$ are averaged over times longer than the correlation time. M_{g} and M_{e} denote the time-dependent number of dye molecules in electronic ground and excited states, respectively. The total number of dye molecules can be written in terms of the ground- and excited-state molecule numbers as: $M = M_{\mathrm{g}} + M_{\mathrm{e}}$, with $M_{\mathrm{g}} = \bar{M}_{\mathrm{g}} + \Delta M_{\mathrm{g}}$ and $M_{\mathrm{e}} = \bar{M}_{\mathrm{e}} + \Delta M_{\mathrm{e}}$. Note also that as the total number of molecules in the cavity is constant, the absolute value of the change in the ground state molecule number is the same with that of the excited state molecule number: $\Delta M_{\mathrm{g}} = -\Delta M_{\mathrm{e}}$. Further, B_{abs} and B_{em} in eqs. (3.1) and (3.2) are the Einstein coefficients for absorption and emission, respectively. For the condensate frequency ω_c and the frequency of the zero-phonon line for the dye ω_{ZPL}, the Einstein coefficients are connected with the Kennard-Stepanov relation, $B_{\mathrm{em}}/B_{\mathrm{abs}} = \exp(-\hbar(\omega_c - \omega_{\mathrm{ZPL}})/k_BT)$. Lastly, κ describes the photon loss rate of the condensate and R_{p} is the pump rate. In the following, we give the solution of the steady state photon number as a function of pump and loss rates.

3.1.1 Steady-state photon number

At the steady state where the particle flow between the condensate and dye molecules is in equilibrium we have $\frac{dn}{dt} = \frac{dM_{\mathrm{e}}}{dt}$ and $\bar{\Delta n} = \Delta\bar{M}_{\mathrm{g}} = 0$. Under these conditions the following set of equations are written:

$$[B_{em}\bar{M}_{\mathrm{e}}(\bar{n}+1) - B_{abs}\bar{M}_{\mathrm{g}}\bar{n}] - \kappa\bar{n} = 0, \tag{3.3a}$$

$$-[B_{em}\bar{M}_{\mathrm{e}}(\bar{n}+1) - B_{abs}\bar{M}_{\mathrm{g}}\bar{n}] + R_{\mathrm{p}}\bar{M}_{\mathrm{g}} = 0. \tag{3.3b}$$

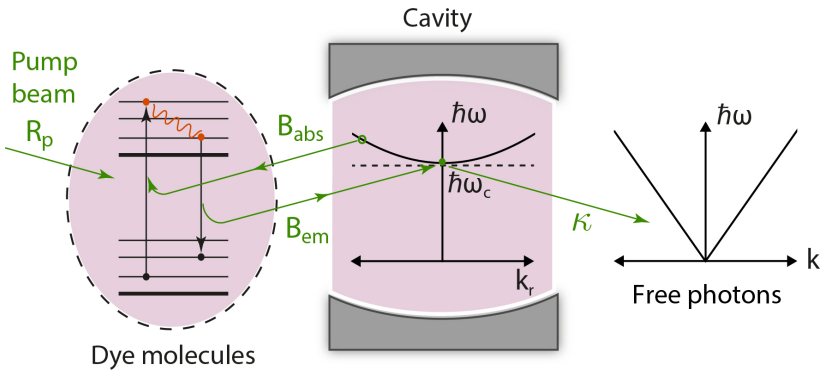

Figure 3.1: Particle flow through the photon gas and the molecular reservoir [73]. A laser beam excites the dye molecules with a photon rate of R_p. The excited molecules thermalise with repeated collisions before they emit the absorbed photon back to the cavity. The optical dispersion in the cavity is quadratic due to the optical confinement. This confinement also induces a minimum allowed energy of the photons, $\hbar\omega_\mathrm{c}$ at the cutoff frequency ω_c in distinction with the free photons. The condensate loses photons e.g. through the mirrors with a rate of κ.

It follows that the mean condensate photon number can be written as a function of the pump rate R_p, loss rate κ and the ground state molecule number $\bar{M}_\mathrm{g}$ as $\bar{n} = \frac{R_\mathrm{p}}{\kappa}\bar{M}_\mathrm{g}$. With the number of ground state molecules much larger than the excited state molecules (approximately two orders of magnitude larger in the experiments described in this study), $M_\mathrm{e} \ll M_\mathrm{g}$ we have

$$\bar{n} \approx \frac{R_\mathrm{p}}{\kappa} M. \tag{3.4}$$

3.1.2 Fluctuations around the steady-state

To describe the dynamics of the fluctuations around the mean photon number, we start with the following set of rate equations derived from eqs. (3.1) and (3.2) for steady state conditions:

$$\begin{aligned}\frac{d(\Delta n)}{dt} &= B_\mathrm{em}(\bar{M}_\mathrm{e} + \Delta M_\mathrm{e})(\bar{n} + \Delta n + 1) \\ &\quad - B_\mathrm{abs}(\bar{M}_\mathrm{g} - \Delta M_\mathrm{e})(\bar{n} + \Delta n) - \kappa(\bar{n} + \Delta n),\end{aligned} \tag{3.5a}$$

$$\begin{aligned}\frac{d(\Delta M_\mathrm{e})}{dt} &= B_\mathrm{abs}(\bar{M}_\mathrm{g} - \Delta M_\mathrm{e})(\bar{n} + \Delta n) \\ &\quad - B_\mathrm{em}(\bar{M}_\mathrm{e} + \Delta M_\mathrm{e})(\bar{n} + \Delta n + 1) + R_\mathrm{p}(\bar{M}_\mathrm{g} - \Delta M_\mathrm{e}).\end{aligned} \tag{3.5b}$$

With steady state conditions $\frac{dn}{dt} = \frac{dM_\mathrm{e}}{dt}$ and neglecting the higher-order terms ($\Delta M_\mathrm{e}\Delta n \approx 0$) eqs. (3.5) simplify to

$$\frac{d(\Delta n)}{dt} = (B_\mathrm{em}\bar{M}_\mathrm{e} - B_\mathrm{abs}\bar{M}_\mathrm{g} - \kappa)\Delta n + (B_\mathrm{em}(\bar{n}+1) - B_\mathrm{abs}\bar{n})\Delta M_\mathrm{e}, \tag{3.6a}$$

$$\frac{d(\Delta M_\mathrm{e})}{dt} = (B_\mathrm{abs}\bar{M}_\mathrm{g} - B_\mathrm{em}\bar{M}_\mathrm{e})\Delta n - (B_\mathrm{em}(\bar{n}+1) + B_\mathrm{abs}\bar{n} + R_\mathrm{p})\Delta M_\mathrm{e}. \tag{3.6b}$$

In Section 2.1.1, for the derivation of the (time-averaged) probability distribution we treated the excitation number as a fixed quantity for a fixed pump rate. In the following discussion, we are interested also in the dynamics of the excitation number for the derivation of the equations of motion for the fluctuations in photon number. We write eqs. (3.6) as a function of the deviation in the excitation number, $\Delta X = \Delta M_{\mathrm{e}} + \Delta n$ and the mean excitation number, $\bar{X} = \bar{M}_{\mathrm{e}} + \bar{n}$. This further simplifies the coupled rate equations to

$$\frac{d(\Delta n)}{dt} = -(B_{\mathrm{em}}\frac{\bar{X}}{\bar{n}} + (B_{\mathrm{em}} + B_{\mathrm{abs}})\bar{n})\Delta n + (B_{\mathrm{em}}(\bar{n}+1) + B_{\mathrm{abs}}\bar{n})\Delta X, \tag{3.7a}$$

$$\frac{d(\Delta X)}{dt} = -\kappa\Delta n - R_{\mathrm{p}}(\Delta X - \Delta n). \tag{3.7b}$$

In the experiments, the condensate photon number is much smaller than the molecule number. In addition, the photon flux between the condensate and the molecules, ΔX and Δn are the same order of magnitude with the photon number. Therefore, the condensate can be sustained by pump rates in the order of $R_{\mathrm{p}} \approx 10^5$ Hz, which is four orders of magnitude smaller than other particle flow rates in the system that are in GHz regime. Accordingly, the pump rate can be neglected; $\frac{d(\Delta X)}{dt} \approx -\kappa\Delta n$. By plugging eqs. (3.7) to each other we obtain

$$\frac{d^2(\Delta n)}{dt^2} + 2\delta\frac{d(\Delta n)}{dt} + \omega_0^2\Delta n = 0, \tag{3.8}$$

where

$$\omega_0^2 = \kappa(B_{\mathrm{em}}(\bar{n}+1) + B_{\mathrm{abs}}\bar{n}), \tag{3.9a}$$

$$\delta = \frac{1}{2}\left(B_{\mathrm{em}}\frac{\bar{X}}{\bar{n}} + (B_{\mathrm{em}} + B_{\mathrm{abs}})\bar{n}\right). \tag{3.9b}$$

Here, ω_0 is a natural oscillation frequency which describes the oscillations without the presence of damping and δ is a damping rate. By substituting the ansatz, $\Delta n = C\exp(\lambda t)$ to the eq. (3.1.2), we obtain $\lambda^2 + 2\delta\lambda + \omega_0^2 = 0$. This equation leads to the general solution of eqs. (3.1):

$$\Delta n = C_1\exp(\lambda_1 t) + C_2\exp(\lambda_2 t), \tag{3.10a}$$

$$\lambda_{1,2} = -\delta \pm \sqrt{\delta^2 - \omega_0^2}. \tag{3.10b}$$

For $\delta < \omega_0$ the eigenvalues $\lambda_{1,2}$ are imaginary and we arrive at oscillatory solutions:

$$\Delta n = \exp(-\delta t)\left[C_1'\sin(\sqrt{\omega_0^2 - \delta^2}\cdot t) + C_2'\cos(\sqrt{\omega_0^2 - \delta^2}\cdot t)\right]. \tag{3.11}$$

By applying the quantum regression theorem [37], the photon-photon correlations that arise due to spontaneous fluctuations in photon number follow the same equations of motion with the relaxation towards the steady state after a small external perturbation. Therefore the second-order correlation

function for the condensate mode is written with the same regression law as eq. (3.11):

$$g^{(2)}(t) - 1 = \exp(-\delta t)\left[C_1' \sin(\sqrt{\omega_0^2 - \delta^2}\cdot t) + C_2' \cos(\sqrt{\omega_0^2 - \delta^2}\cdot t)\right]. \tag{3.12}$$

The results obtained in this section are also derived with a master equation approach in references [73, 95]. The following section covers real eigenvalues which are obtained when the damping rate δ is larger than the natural oscillation frequency ω_0.

3.2 Non-Hermitian fluctuation matrix and the exceptional point

The observed oscillations are expected to be replaced by a biexponential damping at an exceptional point that is reached at a sufficiently small critical photon number. Eqs. (3.7) and (3.9) are written in matrix form as

$$\frac{d}{dt}\begin{pmatrix}\Delta n\\ \Delta X\end{pmatrix} = \hat{A}\begin{pmatrix}\Delta n\\ \Delta X\end{pmatrix} \tag{3.13}$$

with the non-Hermitian matrix

$$\hat{A} = \begin{pmatrix}-2\delta & \omega_0^2/\kappa\\ -\kappa & 0\end{pmatrix}. \tag{3.14}$$

The definitions of the damping rate δ and the natural angular frequency ω_0 are given in eqs. (3.9), and κ is the photon loss rate of the condensate. An exponential ansatz $\Delta n = Ce^{\lambda t}$, leads to the general solution, $\Delta n = C_1 e^{\lambda_1 t} + C_2 e^{\lambda_2 t}$ with constants C_1, C_2 and the matrix eigenvalues $\lambda_{1,2} = -\delta \pm \sqrt{\delta^2 - \omega_0^2}$. The small deviations from the steady state value occur due to the grand canonical character of the system. The coupling of the condensate with the thermal molecular reservoir leads to statistical fluctuations in the photon number. The dynamics that arise from these fluctuations can only be observed in the photon number correlations. As stated in the previous section, since the second-order correlation function describes the expectation value for the small deviations of the photon number, it is possible to apply the quantum regression theorem to relate the second-order correlation function $g^{(2)}(t)$ with an individual instantaneous deviation Δn [37, 72, 73]. The general solution for the second-order correlation is written as $g^{(2)}(t) = 1 + C_1 e^{\lambda_1 t} + C_2 e^{\lambda_2 t}$.

As noted earlier, for the case when damping δ is smaller than the natural frequency ω_0 the eigenvalues $\lambda_{1,2}$ become complex. In this case the solution for the dynamics of the second-order correlation function is a damped oscillation. However, in the opposite case when the damping is larger than the natural frequency $\delta > \omega_0$, the solution is written with two real eigenvalues, describing a biexponential damping; $g^{(2)}(t) = 1 + e^{-\delta t}(C_1' e^{\sqrt{\delta^2-\omega_0^2}t} + C_2' e^{-\sqrt{\delta^2-\omega_0^2}t})$. The change in the dynamics occurs at the exceptional point; $\delta = \omega_0$, where the eigenvalues of the fluctuation matrix coalesce, $\lambda_1 = \lambda_2$ (Figure 3.2).

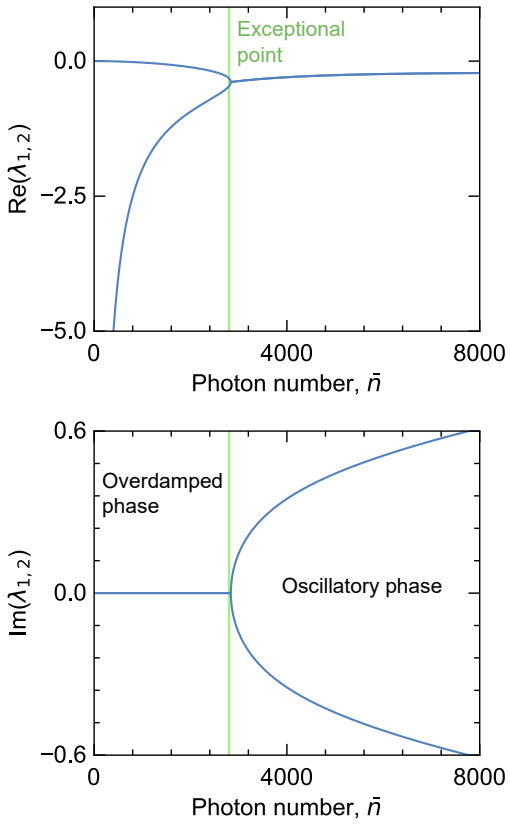

Figure 3.2: Theoretical prediction for real and imaginary eigenvalues. Below a critical mean photon number, the eigenvalues of the fluctuation matrix are real. In this case the dynamics of the fluctuations is overdamped. The two real eigenvalues coalesce at the critical mean photon number, which marks the exceptional point. Above the exceptional point the eigenvalues become imaginary and oscillations appear in the dynamics of the fluctuations.

3.2.1 Solution of the exceptional point and the phase diagram

In this section, the exceptional point is calculated as a function of the loss rate, condensate photon number and the molecule number to construct a phase diagram that distinguishes the expected biexponential and oscillatory behaviors of the correlation function. The exceptional point is reached at $\delta = \omega_0$, with the definitions of the damping rate δ and the natural oscillation frequency ω_0 given in eqs. (3.9). Using the definitions given in eqs. (3.9) at the transition point, $\delta^2 = \omega_0^2$ we write

$$4\kappa \left(B_{\mathrm{em}}(\bar{n}+1) + B_{\mathrm{abs}\bar{n}}\right) = \left(B_{\mathrm{em}} \frac{M_{\mathrm{e}} + \bar{n}}{\bar{n}} + (B_{\mathrm{em}} + B_{\mathrm{abs}})\bar{n}\right)^2 . \tag{3.15}$$

In addition, at the steady state the excited number of molecules is given as

$$M_{\mathrm{e}} = \frac{B_{\mathrm{abs}} M \bar{n} + \kappa \bar{n}}{B_{\mathrm{em}}(\bar{n}+1) + B_{\mathrm{abs}}\bar{n}}. \tag{3.16}$$

By plugging eq. (3.15) in eq. (3.16) we obtain a quadratic relation, which we solve to obtain

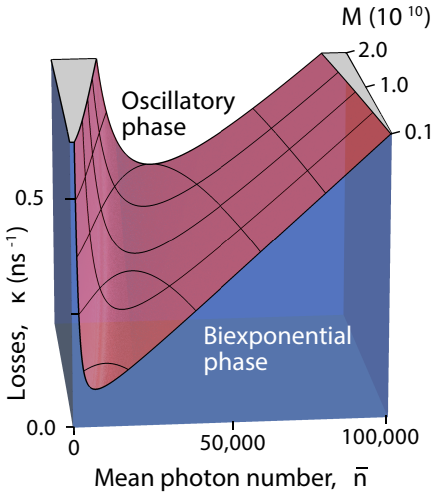

Figure 3.3: Exceptional point induced phase boundary between the biexponential and oscillatory phases calculated by solving $\delta = \omega_0$ as a function of the photon loss rate κ, condensate photon number $\bar{n}$ and the total molecule number M (see eqs. (3.13) [72].

a three dimensional phase diagram for the photon condensate, which is given in Figure 3.3. The structure of the phase diagram depends on the size of the particle reservoir which is quantified by the total molecule number M, the photon number in the condensate $\bar{n}$ and the loss rate κ. In general, biexponential dynamics of the fluctuations is only expected for small losses and a large particle reservoir. Notably, there are two branches of the phase boundary that correspond to the canonical and grand-canonical statistical limits. In Figure 3.3, for a fixed loss rate and total molecule number, the two separate transition points that are reached as the photon number is increased is seen. The first transition point is reached at small mean photon numbers where the photon gas is in grand-canonical statistical conditions ($M_{\mathrm{eff}} \gg \bar{n}^2$). As the photon number is increased, the photon gas is moved towards canonical statistical conditions and a second transition is theoretically expected in this limit. This behavior is seen more clearly by simplifying the solution of the phase boundary (eq. (3.15)) with the approximations of $\bar{n} \gg 1$, $B_{\mathrm{em}} \gg B_{\mathrm{abs}}$ and $M_{\mathrm{e}} \gg \bar{n}$. These approximations are valid in our experimental conditions with 2 orders of magnitude difference between B_{em} and B_{abs} and 5 orders of magnitude difference between M_{e} and $\bar{n}$. The transition point ($\delta = \omega_0$) is reached at $\sqrt{\kappa B_{\mathrm{em}} \bar{n}} \approx \frac{1}{2} B_{\mathrm{em}} \left(\frac{M_{\mathrm{e}}}{\bar{n}} + \bar{n} \right)$. The first term of the sum in the right-hand side is dominant for the case when the condensate is deep in the grand-canonical statistical regime, whereas the second term of the sum is dominant for the opposite case. The first term is interpreted as the gain from the spontaneously emitted photons, and is missing in usual laser theory. Experimentally, the second branching at the canonical case is not reached as the fluctuations diminish at this limit.

With the approximations used above ($B_{\mathrm{em}} \gg B_{\mathrm{abs}}$ and $M_{\mathrm{e}} \gg \bar{n}$), the exceptional point that separates the two phases is written in the form

$$\kappa \approx \frac{1}{4} \left(\frac{(B_{abs} M)^2}{B_{em} \bar{n}^3} + B_{em} \bar{n} \right). \tag{3.17}$$

Next, we find scaled parameters that collapse the 3D phase diagram shown in Figure 3.3 to 2D. The scaling factor f for the photon number $\bar{n}$ is found by equating the two terms in the sum of eq. (3.17), $\frac{(MB_{\mathrm{abs}})^2}{B_{\mathrm{em}}} \cdot \frac{1}{f^3} = B_{\mathrm{em}} f$, which gives $f = \sqrt{M_{\mathrm{e}}}$. Accordingly, a normalized photon number $\bar{\alpha}$ can be defined as $\bar{\alpha} = \bar{n}/M_{\mathrm{e}}$. Figure 3.4 (a) shows the scaled phase diagrams for five different total molecule numbers that are investigated in the current experiments. In this 2D phase diagram with the normalized photon number, we see that as the molecule number is increased the biexponential phase becomes more dominant. In addition, with a scaling with the normalized loss rate $\kappa/(B_{\mathrm{em}}\sqrt{M_{\mathrm{e}}})$, the curves with different total molecule numbers overlap and the phase diagram shown in Figure 3.3 collapses into 2D (Figure 3.4 (b)).

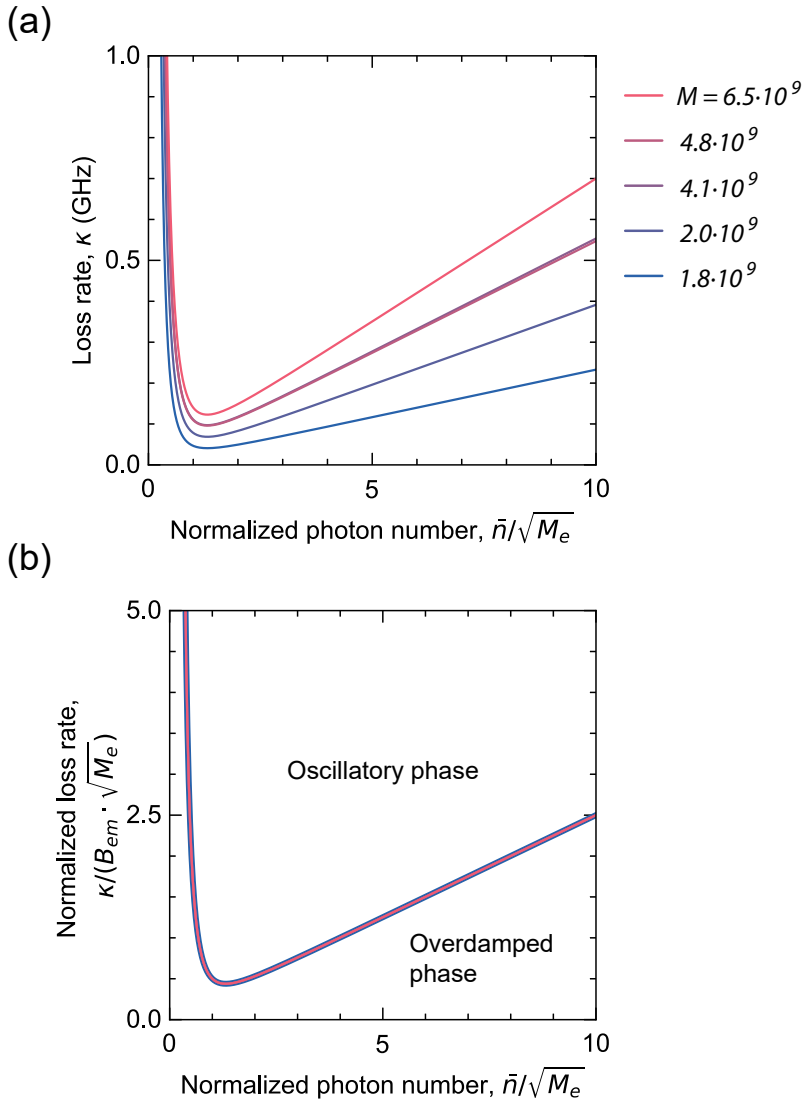

Figure 3.4: Boundary for the biexponential and oscillatory phases calculated with the normalized photon number (a) and with both the normalized photon number and the normalized loss rate (b). Different colors of the curves belong to different total molecule numbers, M that are investigated in the experiments. (b) Applying a scaling factor to the photon number and the loss rate collapses the 3D phase diagram to 2D.

3.2.2 Fit model for the second-order correlation function

In earlier sections, the general solution for the second-order correlation function dynamics were given in the form: $g^{(2)}(t) = 1 + e^{-\delta t}(C_1 e^{\sqrt{\delta^2-\omega_0^2}t} + C_2 e^{-\sqrt{\delta^2-\omega_0^2}t})$. For the case of an overdamped solution $\delta \leq \omega_0$, the constants C_1 and C_2 are real. However for the opposite case with $\delta < \omega_0$, we arrive to the oscillating solution: $g^{(2)}(t) - 1 = e^{-\delta t}\left[a\sin(\sqrt{\omega_0^2-\delta^2}\cdot t) + b\cos(\sqrt{\omega_0^2-\delta^2}\cdot t)\right]$. Here, the constants $a = i(C_1 - C_2)$ and $b = C_1 + C_2$ lead to the imaginary values of $C_{1,2} = \frac{1}{2}(b \pm ia)$. For the fitting of the theoretical model to the experimental data, it is desirable to have free parameters that are both real and continuously tuned across the transition point. For this purpose we define the constants $C_{1,2}$ as

$$C_1 = Y + i\sqrt{\omega_0^2 - \delta^2}Z, \tag{3.18a}$$

$$C_2 = Y - i\sqrt{\omega_0^2 - \delta^2}Z. \tag{3.18b}$$

With this definition, we obtain a model function describing the general solution of the coupled nonlinear equations, where the fit parameters Y, Z, δ, ω_0 are real at both oscillatory and overdamped phases and are continuously tuned across the transition point:

$$g^{(2)}(t) = 1 + e^{-\delta t}\left[(Y + i\sqrt{\omega_0^2 - \delta^2}Z)e^{-\sqrt{\delta^2-\omega_0^2}t} + (Y - i\sqrt{\omega_0^2 - \delta^2}Z)e^{\sqrt{\delta^2-\omega_0^2}t}\right]. \tag{3.19}$$

Therefore, the fit parameters δ, ω_0, Y and Z apply to both phases and the residuals function changes continuously as these fit parameters are tuned. In this way, the inequality relation between the parameters δ and ω_0 obtained from the fit function in eq. (3.19) determine if the curve belongs to an oscillating or biexponential behavior with $\delta > \omega_0$ corresponding to a biexponential, and the opposite case to an oscillating behavior of the second-order coherence function.

3.3 Experiments on the open-system dynamics of the photon gas

For the experiments investigating the open-system dynamics of the photon number fluctuations we used a similar experimental setup as described in Section 2.4. Figure 3.5 shows optical spectrum measurements taken from the cavity emission. The energy distribution of the photons in the cavity agree with the Bose-Einstein distribution expected for the photon gas that is in equilibrium at 300 K within experimental limitations. To investigate the influence of the openness of the system on the statistical number fluctuations, we recorded the time-resolved intensity trace of the condensate photons that leak from the cavity. As explained in Section 2.2, a single detector is sufficient for a photon-photon correlation measurement in contrast with the conventional Hanbury-Brown and Twiss approach that employs two detectors [29]. For the measurement of the average fluctuation amplitude described in Chapter 2, we used a streak camera that allowed a precise filtering of the thermal cloud photons from the condensate photons. For the measurements of the fluctuation dynamics we used an ultra-fast PMT (Photek PMT210) with 5 GHz bandwidth instead of the streak camera. For the measurement of the dynamics, the momentum filtering is not as critical as in the case of of a fluctuation amplitude $g^{(2)}(0)$ measurement. In addition, it is possible to collect the same amount of statistics

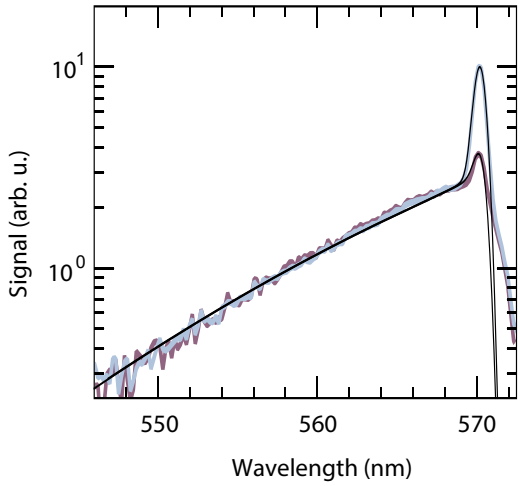

Figure 3.5: Spectra of the Bose-Einstein condensed photon gas recorded from the cavity emission. Energy distribution of condensates with mean photon numbers of $\bar{n} \approx 2100$ (red line) and ≈ 14000 (blue line) agree the expected Bose-Einstein distribution at 300 K (black line). The experimental parameters are the condensate wavelength $\lambda_c \approx 571.3$ nm and the longitudinal mode number $q = 7$.

within a few hours with a PMT measurement, in contrast to several days total measurement times of the streak camera. Therefore, even though the dynamics of the fluctuations were also observable on the streak camera with clear signatures of non-equilibrium observed in their decay as seen in for example, Figure 2.7, we used the fast PMT for a full investigation of the non-Hermitian phases.

The condensate light (TEM_{00} mode) that is transmitted through one of the cavity mirrors was filtered out of the rest of the cavity emission (higher energy modes that comprise the thermal cloud) with two irises that function as a spatial filter and momentum filter, respectively. For this purpose, the cavity emission was passed through a telescope which comprise lenses with focal lengths of 60 mm and 125 mm. The first iris that functions as a spatial filter was placed at the focal plane of the second lens. The light passing through the iris was monitored with a CMOS camera to ensure that photons from the thermal cloud are filtered out. The light passing through the spatial filter was propagated for half a meter and directed to the second iris that functions as the mode filter. The opening of the second iris was adjusted so that approximately 99% of the intensity of the beam is passing through. The light is further polarization filtered to account for the polarization degeneracy of the ground mode (see Figure 2.4, where the PMT used to record the mean electronic traces of condensate pulses is in this case replaced with the ultra-fast PMT for the time-resolved measurements described in this chapter). The remaining single mode photons were focused on the ultra-fast PMT and the signal was recorded with a 3.5 GHz bandwidth oscilloscope (Tektronix DPO 7000C). In general, the high bandwidth measurements come at the cost of electronic noise. The PMT signal was not electronically amplified to avoid additional electronic noise. Further, we reduced the electronic noise by measuring the cross-correlations between two channels that record the intensity trace simultaneously, similar to the approach in a Hanbury-Brown and Twiss experiment [29] but with a single detector. Two main noise channels in our experiments are the background electronic noise and a large bandwidth noise originating from the oscilloscope, which are random in one channel with relative to the other.

Therefore, in a cross-correlation measurement from two independent channels recording the same signal, the majority of the electronic noise is cancelled out and an intensity trace originating purely from the optical signal is resolved.

The PMT signal is calibrated for the mean condensate photon numbers measured from a fit of Bose-Einstein distribution to the optical spectrum (see Figure 3.5). A fraction of the intensity of the higher energy modes still overlap with the optical axis in the far field. Therefore, thermal cloud photons that pass through the iris still contribute to the measurement, lowering the magnitude of the measured photon-photon correlation signal. As a result, the value of the zero-time correlation function, $g^{(2)}(0)$ is smaller than the theoretically expected values. However, the temporal shape of the correlation signal is not affected by this limitation.

In addition to the second-order coherence functions, the average intensity of the condensate mode at the steady state, which is calibrated for the condensate photon number, is measured for each pulse. In this way, second-order correlation functions and their corresponding average condensate photon numbers are recorded over a range of 0 to 15000 condensate photons for 30000 pulses, while the condensate wavelength is fixed. For the analysis of the data, the $g^{(2)}(\tau)$ curves are averaged in bins of 250 photons.

3.3.1 Non-Hermitian dynamics of the second-order correlation function

Typical measured second-order correlation functions for average photon numbers $\bar{n} \approx 4620$ and $\bar{n} \approx 17100$ at a condensate wavelength of $\lambda_c \approx 571.3$ nm are shown in Figure 3.6. As expected from the theoretical analysis given in Section 3.1, a clear damped oscillatory behavior is observed for both condensate sizes. The frequency of these oscillations, Ω_0 were extracted by fitting the solution of the temporal behavior of the second-order correlation function given in eq. (3.12) to the experimental data. We observe that for smaller condensate sizes the oscillations are slower and the oscillation frequency of the second-order correlation function increases as the condensate size is increased. For a mean condensate photon number of $\bar{n} \approx 4620$ the oscillation frequency is $\Omega_0 \approx 2\pi \cdot 0.44$ GHz, whereas it is $\Omega_0 \approx 2\pi \cdot 0.94$ GHz for $\bar{n} \approx 17100$ (Figure 3.6). In addition to the change in the oscillation frequency, the magnitude of the correlation function, i.e. the value of $g^{(2)}(0)$ is also varied as the mean photon number is tuned. The average magnitude of the photon number fluctuations is closely related with the relative size of the particle reservoir and is explained in detail in Chapter 2. In the present experiments the measured values of the zero-delay second-order correlation function are much smaller than the theoretically expected values of $g^{(2)}(0) \approx 2$ and $g^{(2)}(0) \approx 1.3$ for $\bar{n} \approx 4620$ and $\bar{n} \approx 17100$, respectively in this experimental settings. As described in the previous section, the smaller magnitude of the correlation function is attributed to the imperfect filtering of the uncorrelated thermal cloud photons, which reduces the correlation signal. The deviation of the experimental data in Figure 3.6 (a) for small time delays $\tau < 2$ ns is caused by this technical limitation.

Figure 3.7 compares traces of the second-order coherence function at photon numbers of $\bar{n} \approx 2300$ and $\bar{n} \approx 14000$. For the former case with a smaller condensate photon number, a fit of the theoretical model given in eq. (3.19) yields a difference of the damping rate and natural oscillation frequency of $\delta - \omega_0 = 2\pi \cdot 19(\pm 2)$ MHz. As described earlier in Section 3.2.2, a positive value of $\delta - \omega_0$ correspond to a biexponential, or overdamped behavior of the second-order coherence function. We interpret this result as the condensate being in the biexponential phase at a photon number of $\bar{n} \approx 2300$. Relaxation times of $\tau_1 = 1.4$ ns and $\tau_2 = 9.9$ ns were extracted from the fit for this data set (Figure 3.7 (a)). The,

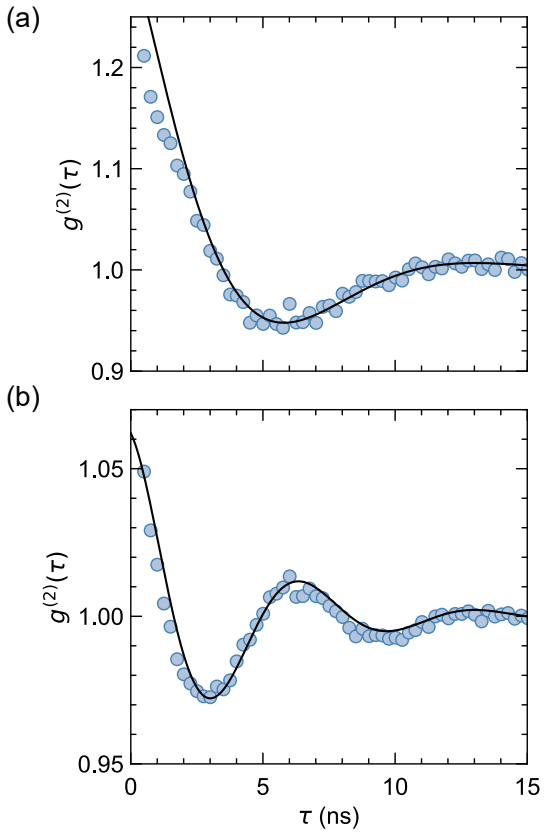

Figure 3.6: Measured second-order correlation functions for mean condensate photon numbers of (a) $\bar{n} \approx 4620$ and (b) $\bar{n} \approx 17100$. Black lines are fits of eq. (3.12) to the experimental data, which yield an oscillation frequency of $\Omega_0 \approx 2\pi \cdot 0.44$ GHz for the smaller and $\Omega_0 \approx 2\pi \cdot 0.94$ GHz for the larger photon number. The experimental parameters are the condensate wavelength $\lambda_c \approx 571.3$ nm and the longitudinal mode number $q = 7$.

$g^{(2)}(\tau)$ trace first decays to below one and then asymptotically approaches one. For the measurement at the larger photon number of $\bar{n} \approx 14000$ on the other hand, an oscillatory signal is observed (Figure 3.7 (b)). In this case the difference of the damping rate and the natural oscillation frequency is negative with $\delta - \omega_0 = -2\pi \cdot 99(\pm 7)$ MHz and the fit converges to an oscillating solution with a single relaxation time of $\tau_c = 3.7$ ns and an oscillation frequency of $\Omega_0 = 2\pi \cdot 0.85 GHz$.

Figure 3.8 shows the difference of the damping rate and the natural oscillation frequency as a function of the condensate photon number, as determined from the fits of the correlation data. For condensate photon numbers below $\bar{n} \approx 2800$, a positive value of the difference, $\delta - \omega_0 > 0$ correspond to real eigenvalues, $\lambda_{1,2} = -\delta \pm \sqrt{\delta^2 - \omega_0^2}$. Above this condensate size however the difference $\delta - \omega_0$ changes sign and $\lambda_{1,2}$ become complex. At this critical photon number of $\bar{n} \approx 2800$, the eigenvalues coalesce, $\lambda_1 = \lambda_2$.

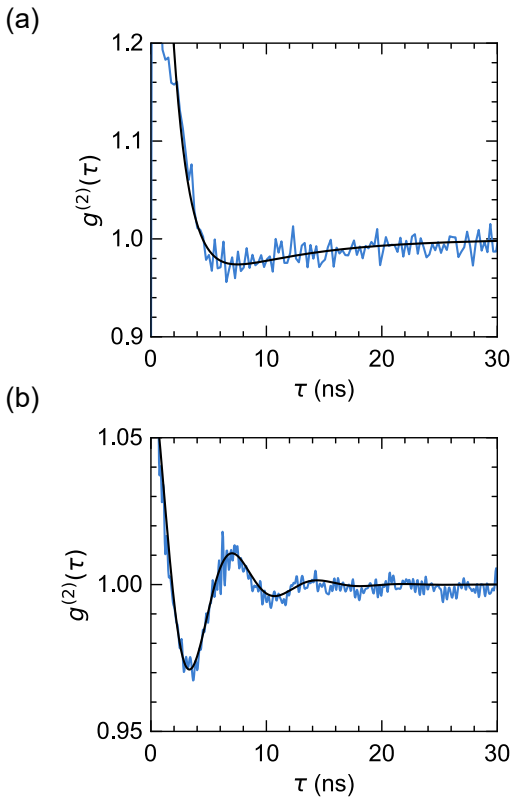

Figure 3.7: Measured second-order correlation functions $g^{(2)}(\tau)$ as a function of time for two different mean photon numbers in the condensate.(a) $g^{(2)}(t)$ decays biexponentially for $\bar{n} \approx 2300$ and (b) with damped oscillations for a larger mean photon number in the condensate: $\bar{n} \approx 14000$. The fits of the theoretical model given in eq. (3.19) to the measured traces are shown in black lines. Experimental parameters are the condensate wavelength $\lambda_c \approx 571.3$ nm and the longitudinal mode number $q = 7$.

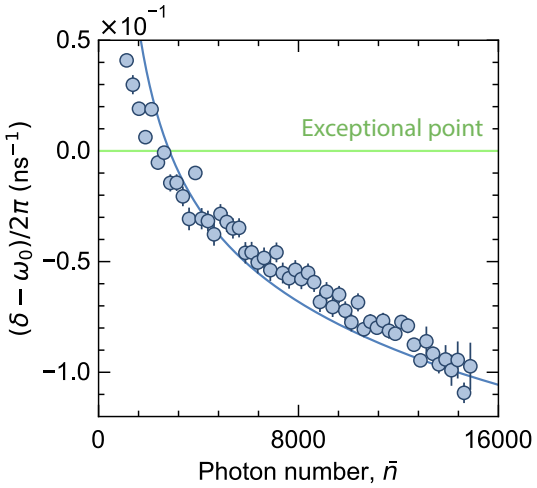

Figure 3.8: The relation between the parameters δ and ω_0 obtained by fitting the theoretical model in eq. (3.19) is used to determine the exceptional point where the eigenvalues, $\lambda_{1,2} = -\delta \pm \sqrt{\delta^2 - \omega_0^2}$ coalesce. The $\lambda_1 = \lambda_2$ condition for the exceptional point is fulfilled at $\delta = \omega_0$, which is reached around a critical photon number of $\bar{n} \approx 2800$ in the current experiments. The experimental parameters are the condensate wavelength $\lambda_c = 571.3$ nm and the longitudinal mode number $q = 7$.

3.3.2 An exceptional point observed in the time scales

The non-Hermitian transition between the two different condensate phases is experimentally mapped by deducing the decay times and, for the oscillatory phase, the oscillation frequency of the second-order correlation function. For this purpose, the mean condensate photon number is tuned while the condensate wavelength and the dye concentration is kept fixed. The obtained times are shown in Figure 3.9. At smaller condensate sizes, which are maintained by weaker pumping and correspondingly weaker losses, we observe that the decay of the second-order coherence has two distinct timescales. Upon tuning the mean condensate photon number to larger values, we observe that the two decay times coalesce. Oscillations in the second-order correlation function emerge at this branching point which occurs around a mean photon number of $\bar{n} \approx 2800$. This critical photon number value marks the transition to the oscillatory dynamics of the second-order coherence.

As described in Section 3.2.1, the assumptions of $B_{\mathrm{em}} \gg B_{\mathrm{abs}}$ and $M_{\mathrm{e}} \gg \bar{n}$ are valid in the used experimental conditions with differences of about 2 and 5 orders of magnitude, respectively. Further, we can write $B_{\mathrm{em}} M_{\mathrm{e}} \approx B_{\mathrm{abs}} M$ at the steady state, as $B_{\mathrm{abs}} M_{\mathrm{g}} \gg \kappa$ with a difference of about 3 orders of magnitude. With these assumptions eqs. (3.9) simplify:

$$\delta \approx \frac{1}{2}\left(\frac{B_{\mathrm{abs}} M}{\bar{n}} + B_{\mathrm{em}}\bar{n}\right), \tag{3.20a}$$

$$\omega_0 \approx \sqrt{\kappa B_{\mathrm{em}}\bar{n}}. \tag{3.20b}$$

The theoretical decay times for the biexponential phase $\tau_{1,2} = 1/(-\delta \pm \sqrt{\delta^2 - \omega_0^2})$, the single decay time for the oscillatory phase $\tau_c = -1/\delta$ and the oscillation frequency $\Omega_0 = \sqrt{\omega_0^2 - \delta^2}$ are calculated from the damping rate δ and the natural oscillation frequency ω_0 defined in eqs. (3.20). The theoretical expressions for the decay times and oscillation frequencies are then fitted to the experimental data (Figure 3.9). Here, the values of B_{abs} and B_{em} are calculated from the literature value of the absorption cross section and Kennard-Stepanov relation at the dye-cavity detuning $\hbar\Delta/k_{\mathrm{B}}T = -4.4$, corresponding to the cutoff wavelength of the measurement $\lambda_c = 571.3$ nm. The loss rate κ and the total molecule number M were used as fit parameters which converged to $\kappa = 2.2(\pm 0.2)$ GHz and $M = 4.76(\pm 0.03) \cdot 10^9$. This larger value of the molecule number compared to the value of $1.5 \cdot 10^8$ obtained in Chapter 2 is attributed to the increased molecular reservoir size, which is expected for the decreased condensate wavelength [35]. The theoretical model agrees well with the experimental data, where the observed deviation of the decay time curve at very small time scales is attributed to the temporal resolution of the used detection system. As a critical photon number is approached from smaller photon numbers, the two characteristic decay times merge towards a single value, and in the case of approaching from larger photon numbers the oscillation frequency converges to zero as the oscillations diminish. This agrees well with the theoretical expectation that at the exceptional point, with $\delta = \omega_0$, the two eigenvalues coalesce $\lambda_1 = \lambda_2$. We interpret this result as evidence that the photon condensate undergoes a non-Hermitian phase transition from the biexponential phase to the oscillatory phase at a critical mean condensate photon number of $\bar{n} \approx 2800$. When the condensate is deep in the biexponential phase, small changes of e.g. mean photon number do not change the correlation function qualitatively. The same is true for a condensate deep in the oscillatory phase. However, at the critical point small variations can lead to a qualitative change.

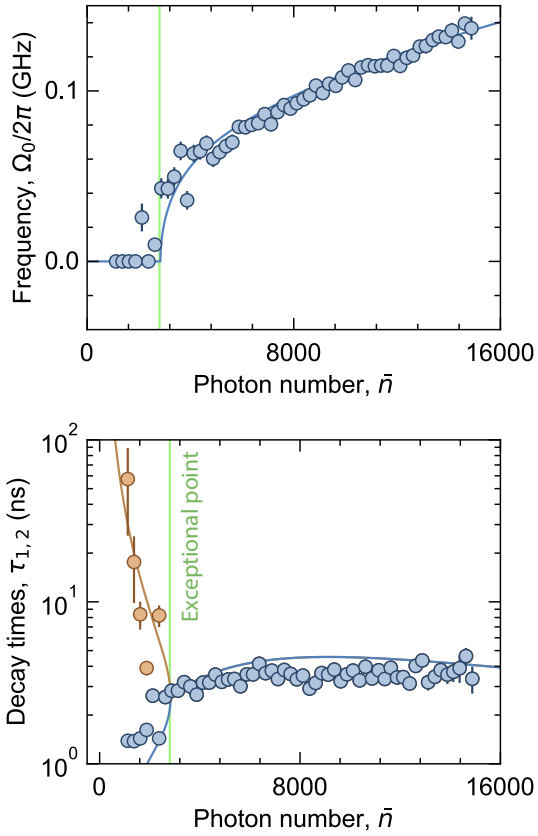

Figure 3.9: Oscillation frequency and decay times of the second-order correlation function $g^{(2)}(\tau)$ as a function of the mean condensate photon number. Solid lines are a fit of the theoretically calculated timescales to the experimental data. Below a critical condensate photon number of $\bar{n} \approx 2800$, the dynamical behavior of the $g^{(2)}(\tau)$ is described by two separate decay times $\tau_{1,2}$ and no oscillation is observed. The critical photon number where the decay times coalesce $\tau_1 = \tau_2$ and oscillations emerge marks the exceptional point. The parameters are the condensate wavelength $\lambda_c = 571.3$ nm, the longitudinal mode number $q = 7$, the loss rate $\kappa = 2.2(\pm 0.2)$ GHz and the total molecule number $M = 4.76(\pm 0.03) \cdot 10^9$.

3.3.3 Exploring the phase diagram

To investigate the boundary between the biexponential and oscillatory phases experimentally in more detail, we measured the second-order correlation function at different condensate wavelengths and dye concentrations. As the condensate wavelength is changed, the values of both the loss rate κ and the Einstein coefficients B_{em} and B_{abs} vary due to the wavelength dependence of the mirror reflectivity and the absorption and emission spectra of the fluorescent dye, respectively. In Section 3.2.1, a dimensionless normalized photon number, $\bar{n}/\sqrt{M_{\mathrm{e}}}$ and loss rate, $\kappa/(B_{\mathrm{em}}\sqrt{M_{\mathrm{e}}})$ was introduced. With these normalisations, the three dimensional phase diagram shown in Figure 3.3 collapses to two dimensions. The measurements at different loss rates and molecule numbers map out the collapsed two dimensional phase diagram (Figure 3.10). In Figure 3.10, the phases corresponding to individual $g^{(2)}(t)$ measurements are shown in red and blue dots for the biexponential and oscillatory regimes, respectively. As also explained in Section 3.2.1, there are two branches of the phase boundary which correspond to the grand-canonical and canonical statistical limits. As seen in Figure 3.3, for a fixed scaled loss rate as the scaled photon number is increased the condensate first goes through the grand-canonical branch of the phase boundary from the biexponential phase to the oscillatory phase. If the photon number is increased further a second transition back into the biexponential phase is expected. However, at the very large photon numbers where where this second transition is expected, the condensate is deeply in the canonical statistical regime. At this regime, the fluctuations of the condensate completely diminish and their dynamics are not seen in correlation measurements. The fit parameters and the experimental parameters for the recorded data points are summarized in Appendix B. The observed phase boundary is in good agreement with the theoretical expectations within the investigated experimental range.

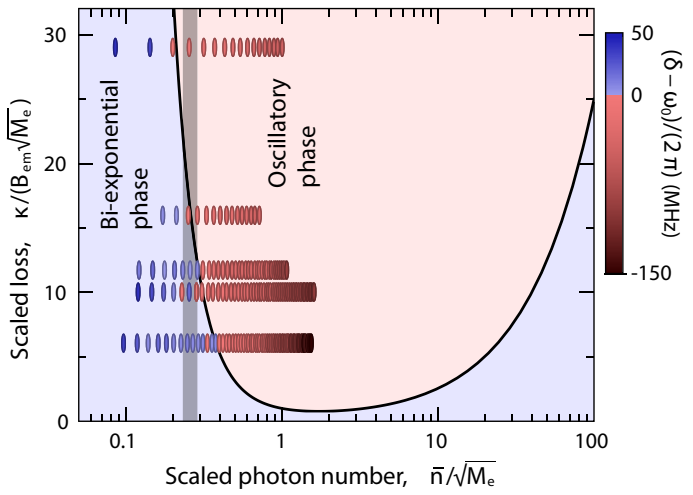

Figure 3.10: Normalized phase diagram and measurements of the non-Hermitian phases corresponding to individual $g^{(2)}(t)$ measurements [72]. The biexponential (red dots) and oscillatory (blue dots) phases are determined from the relation between the damping rate δ and the natural oscillation frequency ω_0, which is used as the criterion for the phase determination (shown in color scale). The phase boundary (black line) is mapped out by measuring the dynamics of the fluctuations at different condensate wavelengths and total molecule numbers. The parameters are given in Appendix B.

3.3.4 Dependence of the time scales to the loss rate at a fixed photon number

In this section we describe the case when the loss rate of the condensate is tuned, moving the system in the direction of an idealized photon box or towards a more open-system setting. For this purpose we fixed the photon number and investigated the oscillation frequency and decay times as a function of the loss rate. As in the case of the phase boundary, the time scales of the dynamics depend on the condensate wavelength and total molecule number. Moreover, as we tune the loss rate by varying the condensate wavelength, we also involuntarily change the total molecule number that the condensate interacts with during the experiments. Therefore to look at the dynamics as we change only the loss rate, we used scaled parameters and plotted the normalized oscillation frequency and the normalized decay times. For a normalized loss rate $\kappa_N = \kappa/(B_{\mathrm{em}} \cdot \sqrt{M_{\mathrm{e}}})$ and normalized photon number $\bar{\alpha} = \bar{n}/\sqrt{M_{\mathrm{e}}}$, δ and ω_0 from eqs. 3.20 are written as

$$\delta(\bar{\alpha}) = \frac{1}{2} B_{\mathrm{em}} \sqrt{M_{\mathrm{e}}} \left(\frac{1}{\bar{\alpha}} + \bar{\alpha}\right), \tag{3.21a}$$

$$\omega_0(\bar{\alpha}, \kappa_N) = B_{\mathrm{em}} \sqrt{M_{\mathrm{e}}} \sqrt{\kappa_N \bar{\alpha}}. \tag{3.21b}$$

Accordingly, normalized oscillation frequency and decay times, where the dependence to the condensate wavelength and the changing reservoir size is lifted are written as

$$\tau_N = \tau B_{\mathrm{em}} \sqrt{M_{\mathrm{e}}}, \tag{3.22a}$$

$$\Omega_N = \Omega/(B_{\mathrm{em}} \sqrt{M_{\mathrm{e}}}). \tag{3.22b}$$

The dependence of the normalized oscillation frequency and decay times to the loss rate at a fixed normalized photon number of $\bar{\alpha} \approx 0.27$ number is shown in Figure 3.11. The gray region in Figure 3.10 marks this normalized photon number. The fit parameters and the experimental parameters for the recorded data points are summarized in Appendix B. The results in Figure 3.11, demonstrate the effect of the openness of the system to the environment, quantified by the photon losses. The biexponential phase observed for small losses is qualitatively different from the (more open) photon condensate in the oscillatory phase. The oscillatory dynamics of the latter case crosses over to the relaxation oscillations of the laser if the losses are increased further about three orders of magnitude (to reach the values of the thermalisation rate: $M_{\mathrm{g}} B_{\mathrm{abs}} \approx 2$ THz).

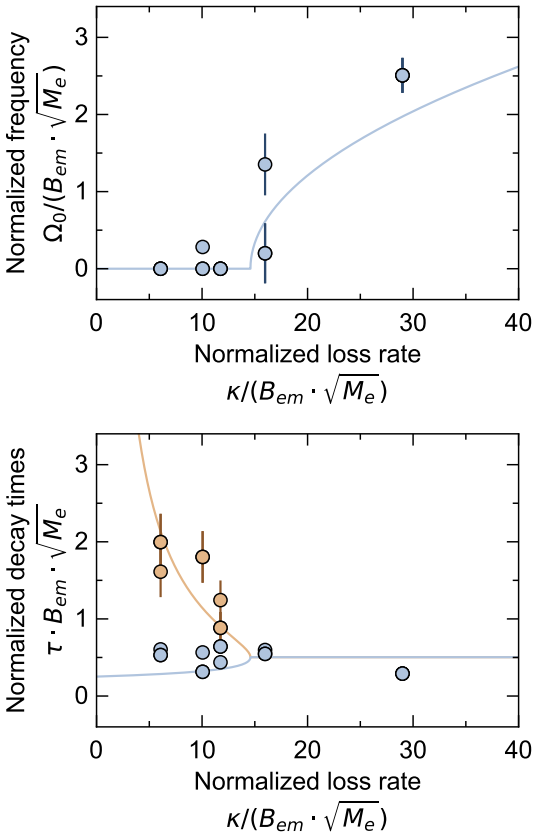

Figure 3.11: The dependence of the second-order correlation function timescales to loss rate at a fixed normalized photon number of $\bar{\alpha} = 0.27$. The solid lines are the theoretical calculations of timescales as given in eqs. (3.22).

3.4 Discussion

Lasing and photon Bose-Einstein condensation both exhibit collective behavior of photons with macroscopic occupation of a quantum state. In addition, both exhibit a broken time-reversal symmetry suggesting that no sharp boundary exist between the two phenomena [93]. Contrary to this perception, the findings in this chapter demonstrate a hierarchy of non-Hermitian phases connecting equilibrium photon Bose-Einstein condensation to non-equilibrium lasing operation (Figure 3.12). When the photon flow through the condensate is small, which happens at small condensate photon numbers or small photon losses, the temporal decay of the second-order correlation function is an exponential decay with two separate time constants. As the photon flow is increased, this biexponential decay ceases at an exceptional point where the two time constants coalesce. The exceptional point marks a non-Hermitian phase transition to an oscillatory behavior of the second-order correlation function. If the rate of the photon flow is increased further, this oscillatory behavior in the thermalised photon gas crosses over to the relaxation oscillations known in laser dynamics [96]. We regard this as evidence that the newly observed biexponential dynamics constitute a state of the photon condensate which is

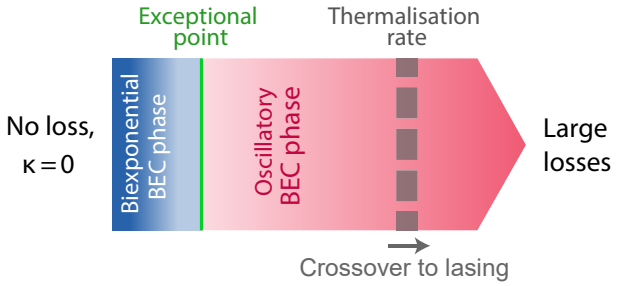

Figure 3.12: Dissipative phases that appear as the losses of a Bose-Einstein condensate of photons is altered. In a weakly dissipative setting, the second-order correlation dynamics of a Bose-Einstein condensate is biexponential. As the losses are increased, the exceptional point is reached and oscillatory dynamics appear. For loss rates above the thermalisation rate, the oscillatory phase crosses over to lasing regime [72].

qualitatively different from the lasing operation.

At the exceptional point, the thermalisation rate is still about three orders of magnitude larger than the photon loss rate with $\kappa/M_g B_{\mathrm{abs}} \approx 1.1 \cdot 10^{-3}$. This means that the phase transition occurs inside the Bose-Einstein condensation regime. Oscillatory dynamics in the correlations has been previously observed in different non-equilibrium systems [97–99]. Distinctly, our results show that equilibrium and non-equilibrium features coexist in the condensate. The energy distribution of the photon condensate agrees with Bose-Einstein distribution expected from thermal equilibrium and the photon number fluctuates due to the coupling with the dye-reservoir. However, dissipative structures in the temporal behavior of the second-order correlation function is observed due to the openness of the photon gas to the environment.

CHAPTER 4

Outlook

A Bose-Einstein condensate of photons realized in our experiments is not completely isolated from its surroundings. It is both statistically coupled to photo-excitable molecules and has a residual openness due to photon losses. In this study, we investigated the fluctuations in the condensate photon number as we systematically changed these two environmental conditions. By changing the relative size of the particle reservoir and the condensate, the amplitude of the fluctuations are tuned between the limits of grand-canonical and canonical statistical ensembles. In the grand-canonical limit, our measurements of the zero-delay second-order correlation function yielded a value of $g^{(2)}(0) \approx 2$, overcoming the limitations from mode filtering of previous experiments [35]. Photon bunched, single-mode light sources have potential applications in quantum imaging [100] and methods to produce such sources include for example, Doppler-shifted, scattered light in gas cells [101]. Here, we obtained light with these features by macroscopic occupation of the ground state by condensation.

One of the main objectives of this study was to verify the fluctuation-dissipation relation for a Bose-Einstein condensate. We experimentally showed that the fluctuation-dissipation relation holds for a Bose-Einstein condensed photon gas in the grand-canonical ensemble conditions. Moreover we observed that if the condensate is tuned towards the canonical ensemble regime, the response of the condensate to a changing chemical potential diverges and in this case the fluctuation-dissipation relation does not hold. In this sense, the divergence of the response function $d\bar{n}/d\mu$ marks a boundary between the two ensemble limits. We further derived and experimentally verified a generalized version of the fluctuation-dissipation relation that is valid both in canonical and grand-canonical statistical limits. In the generalized response function, the chemical potential is replaced by the dye-cavity detuning which directly controls the coupling of the condensate and the molecular reservoir.

It is particularly interesting that the observed agreement with the fluctuation-dissipation theorem occurs under the residual photon losses of the condensate. Generalization of fluctuation-dissipation relations to non-equilibrium conditions is an actively pursued goal [102] and is useful for studies such as the investigation of the tunneling time via the quantum shot noise [103]. In the weakly driven-dissipative settings realized in our experiments, we observed no significant effect of this non-equilibrium character to the amplitude of the fluctuations, whereas the dynamics of the fluctuations was strongly altered. In general, a tuneability between in- and out-of-equilibrium conditions help to investigate both non-equilibrium [86, 87, 104] and equilibrium [89, 105] phenomena. The tuneability of photon condensates between the equilibrium and far-from equilibrium limits [10, 18, 26, 72, 106, 107] is promising for further studies of fluctuation-dissipation relations in non-equilibrium scenarios.

Our findings demonstrated that even a very small deviation from the idealized closed system can lead to non-Hermitian phases in the dynamics of the fluctuations. They also led to the understanding of a hierarchy of dissipative phases that connect Bose-Einstein condensation and lasing. At the single particle level the same mechanism drives the formation of a Bose-Einstein condensate and the operation of a laser: an increased rate of scattering or emission to a given state that is already populated with other identical Bose particles [108, 109]. This enhancement factor is due to the symmetric wavefunctions of Bose particles and is the origin of the amplification of light in a laser as well as of matter wave amplification in a Bose-Einstein condensate [7, 110, 111]. Despite this connection, the quantum statistics describing these two phenomena are very different. Bose-Einstein condensation is a phenomenon which occurs in thermal equilibrium and the particles follow the Bose-Einstein distribution. Lasing, on the other hand, is an intrinsically non-equilibrium process where the system is open to the environment with constant pumping and losses. Several studies have found a crossover-like transition between the two extreme regimes of equilibrium condensation and laser operation [35, 112, 113], whereas recent theoretical work suggested the existence of a non-Hermitian phase transition between the two phenomena [41]. In this thesis we demonstrated a new dissipative state of a photon Bose-Einstein condensate which is separated from both lasing and a second, more lossy condensate state with a non-Hermitian phase transition.

Further promising future directions include new topological phases that are expected to occur in lattices of coupled, driven-dissipative photon condensates [42, 51, 114–118]. Another actively studied direction is the development of new quantum computing methods using photon condensates [119, 120]. In different quantum many-body systems, examples of dissipatively prepared states include Mott insulators [118] and entangled quantum states [121]. In addition, the sensitivity of non-Hermitian systems near an exceptional point has been utilized in the development of ultra-sensitive gyroscopes [78, 122] and suggested for enhanced energy harvesting [123]. Finally, we would like to remark that most real-life systems do not fit in idealized scenarios we use to develop physical models. A perfect isolation from the environment is such an idealized scenario. Understanding the effect of a coupling of the system to the environment, as systematically done in our studies, is essential for more accurate models of dissipative quantum gases and to develop applications that utilize dissipation.

Bibliography

[1] S. N. Bose, O. Theimer and B. Ram, *The beginning of quantum statistics: A translation of"Planck's law and the light quantum hypothesis"*, American Journal of Physics **44** (1976) 1056 (cit. on p. 1).

[2] A. Pais, *Subtle is the Lord : The Science and the Life of Albert Einstein*, Oxford University Press, USA, 1982, ISBN: 9780191524028, URL: https://books.google.nl/books?id=KdaiZDaB7TgC (cit. on p. 1).

[3] A. Einstein, *Quantentheorie des einatomigen idealen gases. zweite abhandlung*, Albert Einstein: Akademie-Vorträge: Sitzungsberichte der Preußischen Akademie der Wissenschaften 1914–1932 (2005) 245 (cit. on pp. 1, 7).

[4] M. H. Anderson et al., *Observation of Bose-Einstein condensation in a dilute atomic vapor*, science **269** (1995) 198 (cit. on p. 1).

[5] K. B. Davis et al., *Bose-Einstein condensation in a gas of sodium atoms*, Physical review letters **75** (1995) 3969 (cit. on p. 1).

[6] C. J. Pethick and H. Smith, *Bose–Einstein condensation in dilute gases*, Cambridge university press, 2008 (cit. on p. 1).

[7] W. Ketterle, *Nobel lecture: When atoms behave as waves: Bose-Einstein condensation and the atom laser*, Reviews of Modern Physics **74** (2002) 1131 (cit. on pp. 1, 2, 60).

[8] J. Kasprzak et al., *Bose–Einstein condensation of exciton polaritons*, Nature **443** (2006) 409 (cit. on pp. 1, 37).

[9] R. Balili et al., *Bose-Einstein condensation of microcavity polaritons in a trap*, Science **316** (2007) 1007 (cit. on p. 1).

[10] J. Klaers et al., *Bose–Einstein condensation of photons in an optical microcavity*, Nature **468** (2010) 545 (cit. on pp. 1, 6–8, 11, 20, 59).

[11] J. Marelic and R. Nyman, *Experimental evidence for inhomogeneous pumping and energy-dependent effects in photon Bose-Einstein condensation*, Physical Review A **91** (2015) 033813 (cit. on p. 1).

[12] S. Greveling, K. Perrier and D. van Oosten, *Density distribution of a Bose-Einstein condensate of photons in a dye-filled microcavity*, Physical Review A **98** (2018) 013810 (cit. on p. 1).

[13] T. K. Hakala et al., *Bose–Einstein condensation in a plasmonic lattice*, Nature Physics **14** (2018) 739 (cit. on p. 1).

[14] R. Weill et al.,
Bose–Einstein condensation of photons in an erbium–ytterbium co-doped fiber cavity,
Nature communications **10** (2019) 1 (cit. on p. 1).

[15] S. Barland et al., *Photon thermalization and a condensation phase transition in an electrically pumped semiconductor microresonator*, Optics Express **29** (2021) 8368 (cit. on p. 1).

[16] J. Klaers et al., *Statistical physics of Bose-Einstein-condensed light in a dye microcavity*, Physical review letters **108** (2012) 160403 (cit. on pp. 2–5, 8, 11, 13, 27).

[17] J. Klaers, *The thermalization, condensation and flickering of photons*,
Journal of Physics B: Atomic, Molecular and Optical Physics **47** (2014) 243001 (cit. on pp. 2–4, 6, 8, 11, 20, 27).

[18] J. Schmitt et al.,
Thermalization kinetics of light: From laser dynamics to equilibrium condensation of photons,
Physical Review A **92** (2015) 011602 (cit. on pp. 2, 7, 9, 59).

[19] P. Kirton and J. Keeling, *Nonequilibrium model of photon condensation*,
Physical review letters **111** (2013) 100404 (cit. on p. 2).

[20] R. Feynman, R. Leighton and M. Sands, *The Feynman Lectures on Physics, Vol. III: The New Millennium Edition: Quantum Mechanics*, The Feynman Lectures on Physics,
Basic Books, 2011, ISBN: 9780465025015,
URL: https://books.google.nl/books?id=KsnbNL%5C_rh04C (cit. on p. 2).

[21] H. R. Lewis, *Einstein's Derivation of Planck's Radiation Law*,
American Journal of Physics **41** (1973) 38 (cit. on p. 3).

[22] R. T. Ross, *Some thermodynamics of photochemical systems*,
The Journal of Chemical Physics **46** (1967) 4590 (cit. on p. 4).

[23] D. McCumber, *Einstein relations connecting broadband emission and absorption spectra*,
Physical Review **136** (1964) A954 (cit. on p. 4).

[24] T. Meyer and T. Markvart, *The chemical potential of light in fluorescent solar collectors*,
Journal of applied physics **105** (2009) 063110 (cit. on pp. 4, 5).

[25] C. Kittel and H. Kroemer, *Thermal physics*, vol. 9690, Wiley New York, 1970 (cit. on p. 5).

[26] J. Klaers, F. Vewinger and M. Weitz,
Thermalization of a two-dimensional photonic gas in a 'white wall'photon box,
Nature Physics **6** (2010) 512 (cit. on pp. 7, 8, 20, 59).

[27] T. Damm et al., *Calorimetry of a Bose–Einstein-condensed photon gas*,
Nature communications **7** (2016) 1 (cit. on p. 7).

[28] C. Kittel, *Elementary statistical physics*, Courier Corporation, 2004 (cit. on pp. 7, 8, 14).

[29] R. H. Brown and R. Q. Twiss, *Correlation between photons in two coherent beams of light*,
Nature **177** (1956) 27 (cit. on pp. 7, 17–19, 46, 47).

[30] M. Schellekens et al., *Hanbury Brown Twiss effect for ultracold quantum gases*,
Science **310** (2005) 648 (cit. on p. 7).

[31] T. Jeltes et al., *Comparison of the Hanbury Brown–Twiss effect for bosons and fermions*, Nature **445** (2007) 402 (cit. on p. 7).

[32] S. Hodgman et al., *Direct measurement of long-range third-order coherence in Bose-Einstein condensates*, Science **331** (2011) 1046 (cit. on p. 7).

[33] P. R. Berman, C. C. Lin and E. Arimondo, *Volume 53 of the Advances in Atomic, Molecular, and Optical Physics*, Elsevier, 2006 (cit. on p. 7).

[34] M. Holthaus, E. Kalinowski and K. Kirsten, *Condensate fluctuations in trapped Bose gases: Canonical vs. microcanonical ensemble*, Annals of Physics **270** (1998) 198 (cit. on p. 7).

[35] J. Schmitt et al., *Observation of grand-canonical number statistics in a photon Bose-Einstein condensate*, Physical review letters **112** (2014) 030401 (cit. on pp. 8, 9, 11, 13, 23, 24, 27, 31, 52, 59, 60).

[36] J. Schmitt, *Dynamics and correlations of a Bose–Einstein condensate of photons*, Journal of Physics B: Atomic, Molecular and Optical Physics **51** (2018) 173001 (cit. on pp. 8, 20, 24, 27, 31).

[37] D. Chandler, *Introduction to modern statistical mechanics*, Oxford university press, 1987 (cit. on pp. 8, 40, 41).

[38] J. S. Lamb and J. A. Roberts, *Time-reversal symmetry in dynamical systems: a survey*, Physica D: Nonlinear Phenomena **112** (1998) 1 (cit. on p. 8).

[39] R. El-Ganainy et al., *Non-Hermitian physics and PT symmetry*, Nature Physics **14** (2018) 11 (cit. on pp. 8, 9).

[40] M.-A. Miri and A. Alu, *Exceptional points in optics and photonics*, Science **363** (2019) (cit. on pp. 8, 9, 37).

[41] R. Hanai et al., *Non-Hermitian phase transition from a polariton Bose-Einstein condensate to a photon laser*, Physical review letters **122** (2019) 185301 (cit. on pp. 8, 9, 37, 60).

[42] K. Kawabata et al., *Symmetry and topology in non-Hermitian physics*, Physical Review X **9** (2019) 041015 (cit. on pp. 8, 60).

[43] I. Prigogine, *Time, structure, and fluctuations*, Science **201** (1978) 777 (cit. on pp. 8, 9).

[44] G. Schoner and J. Kelso, *Dynamic pattern generation in behavioral and neural systems*, Science **239** (1988) 1513 (cit. on pp. 8, 9).

[45] G. Makey et al., *Universality of dissipative self-assembly from quantum dots to human cells*, Nature Physics **16** (2020) 795 (cit. on pp. 9, 37).

[46] H. Haken, *Cooperative phenomena in systems far from thermal equilibrium and in nonphysical systems*, Reviews of modern physics **47** (1975) 67 (cit. on p. 9).

[47] T. Kato, *Perturbation theory for linear operators*, vol. 132, Springer Science & Business Media, 2013 (cit. on pp. 9, 37).

[48] C. M. Bender and S. Boettcher,
Real spectra in non-Hermitian Hamiltonians having P T symmetry,
Physical Review Letters **80** (1998) 5243 (cit. on pp. 9, 37).

[49] T. Gao et al.,
Observation of non-Hermitian degeneracies in a chaotic exciton-polariton billiard,
Nature **526** (2015) 554 (cit. on p. 9).

[50] F. Minganti et al., *Quantum exceptional points of non-Hermitian Hamiltonians and Liouvillians: The effects of quantum jumps*, Physical Review A **100** (2019) 062131 (cit. on p. 9).

[51] R. Hanai and P. B. Littlewood, *Critical fluctuations at a many-body exceptional point*, Physical Review Research **2** (2020) 033018 (cit. on pp. 9, 37, 60).

[52] A. Einstein, *On the movement of small particles suspended in stationary liquids required by the molecularkinetic theory of heat*, Ann. d. Phys **17** (1905) 1 (cit. on pp. 11, 36).

[53] J. B. Johnson, *Thermal agitation of electricity in conductors*, Physical review **32** (1928) 97 (cit. on p. 11).

[54] H. Oukris and N. Israeloff, *Nanoscale non-equilibrium dynamics and the fluctuation–dissipation relation in an ageing polymer glass*, Nature Physics **6** (2010) 135 (cit. on p. 11).

[55] T. Müller et al., *Local observation of antibunching in a trapped Fermi gas*,
Physical review letters **105** (2010) 040401 (cit. on p. 11).

[56] J. Esteve et al., *Observations of density fluctuations in an elongated Bose gas: Ideal gas and quasicondensate regimes*, Physical review letters **96** (2006) 130403 (cit. on p. 11).

[57] M. Kristensen et al., *Observation of atom number fluctuations in a Bose-Einstein condensate*,
Physical review letters **122** (2019) 163601 (cit. on p. 11).

[58] R. Baierlein, *The elusive chemical potential*, American Journal of Physics **69** (2001) 423 (cit. on pp. 11, 34).

[59] H. S. Leff, *Fluctuations in particle number for a photon gas*,
American Journal of Physics **83** (2015) 362 (cit. on pp. 11, 34, 36).

[60] A. Chiocchetta, A. Gambassi and I. Carusotto,
Laser operation and Bose-Einstein condensation: analogies and differences,
arXiv preprint arXiv:1503.02816 (2015) (cit. on p. 12).

[61] J. Schmitt, *Private communication*, () (cit. on p. 12).

[62] R. H. Brown and R. Q. Twiss, *A test of a new type of stellar interferometer on Sirius*,
Nature **178** (1956) 1046 (cit. on pp. 17, 19).

[63] H. J. Kimble, M. Dagenais and L. Mandel, *Photon antibunching in resonance fluorescence*,
Physical Review Letters **39** (1977) 691 (cit. on pp. 17, 19).

[64] P. Grangier, G. Roger and A. Aspect, *Experimental evidence for a photon anticorrelation effect on a beam splitter: a new light on single-photon interferences*,
EPL (Europhysics Letters) **1** (1986) 173 (cit. on pp. 17–19).

[65] R. Loudon, *The quantum theory of light*, OUP Oxford, 2000 (cit. on p. 18).

[66] E. M. Purcell, *The question of correlation between photons in coherent light rays*, Nature **178** (1956) 1449 (cit. on p. 18).

[67] J. Garrison and R. Chiao, *Quantum optics*, Oxford University Press, 2008 (cit. on p. 18).

[68] J. Wiersig et al., *Direct observation of correlations between individual photon emission events of a microcavity laser*, Nature **460** (2009) 245 (cit. on p. 19).

[69] M. Aßmann et al., *Higher-order photon bunching in a semiconductor microcavity*, Science **325** (2009) 297 (cit. on p. 19).

[70] M. Aßmann et al., *Measuring the dynamics of second-order photon correlation functions inside a pulse with picosecond time resolution*, Optics express **18** (2010) 20229 (cit. on pp. 19, 69).

[71] G. A. Steudle et al., *Measuring the quantum nature of light with a single source and a single detector*, Physical Review A **86** (2012) 053814 (cit. on pp. 18, 19).

[72] F. E. Öztürk et al., *Observation of a non-Hermitian phase transition in an optical quantum gas*, Science **372** (2021) 88 (cit. on pp. 27, 37, 38, 41, 43, 54, 57, 59).

[73] F. E. Ozturk et al., *Fluctuation dynamics of an open photon Bose-Einstein condensate*, Physical Review A **100** (2019) 043803 (cit. on pp. 27, 37, 39, 41).

[74] B. T. Walker et al., *Non-stationary statistics and formation jitter in transient photon condensation*, Nature communications **11** (2020) 1 (cit. on p. 37).

[75] Ş. K. Özdemir et al., *Parity–time symmetry and exceptional points in photonics*, Nature materials **18** (2019) 783 (cit. on p. 37).

[76] T. Fink et al., *Signatures of a dissipative phase transition in photon correlation measurements*, Nature Physics **14** (2018) 365 (cit. on p. 37).

[77] I. Prigogine, *Time, structure, and fluctuations*, Science **201** (1978) 777 (cit. on p. 37).

[78] Y.-H. Lai et al., *Observation of the exceptional-point-enhanced Sagnac effect*, Nature **576** (2019) 65 (cit. on pp. 37, 60).

[79] S. Diehl et al., *Quantum states and phases in driven open quantum systems with cold atoms*, Nature Physics **4** (2008) 878 (cit. on p. 37).

[80] D. Sels and E. Demler, *Thermal radiation and dissipative phase transition in a BEC with local loss*, Annals of Physics **412** (2020) 168021 (cit. on p. 37).

[81] E. Altman et al., *Two-dimensional superfluidity of exciton polaritons requires strong anisotropy*, Physical Review X **5** (2015) 011017 (cit. on p. 37).

[82] F. Ferri et al., *Emerging dissipative phases in a superradiant quantum gas with tunable decay*, arXiv preprint arXiv:2104.12782 (2021) (cit. on p. 37).

[83] N. Dogra et al.,
Dissipation-induced structural instability and chiral dynamics in a quantum gas,
Science **366** (2019) 1496 (cit. on p. 37).

[84] I. Bloch, J. Dalibard and W. Zwerger, *Many-body physics with ultracold gases*,
Reviews of modern physics **80** (2008) 885 (cit. on p. 37).

[85] P. Comaron et al., *Dynamical critical exponents in driven-dissipative quantum systems*,
Physical review letters **121** (2018) 095302 (cit. on p. 37).

[86] A. Zamora et al., *Tuning across universalities with a driven open condensate*,
Physical Review X **7** (2017) 041006 (cit. on pp. 37, 59).

[87] D. Vorberg, R. Ketzmerick and A. Eckardt, *Unified theory for excited-state, fragmented, and equilibriumlike Bose condensation in pumped photonic many-body systems*,
Physical Review A **97** (2018) 063621 (cit. on pp. 37, 59).

[88] T. Byrnes, N. Y. Kim and Y. Yamamoto, *Exciton–polariton condensates*,
Nature Physics **10** (2014) 803 (cit. on p. 37).

[89] Y. Sun et al., *Bose-Einstein condensation of long-lifetime polaritons in thermal equilibrium*,
Physical review letters **118** (2017) 016602 (cit. on pp. 37, 59).

[90] A. Amo et al., *Superfluidity of polaritons in semiconductor microcavities*,
Nature Physics **5** (2009) 805 (cit. on p. 37).

[91] K. G. Lagoudakis et al., *Quantized vortices in an exciton–polariton condensate*,
Nature physics **4** (2008) 706 (cit. on p. 37).

[92] W. Heiss, *Exceptional points of non-Hermitian operators*,
Journal of Physics A: Mathematical and General **37** (2004) 2455 (cit. on p. 37).

[93] A. Griffin, D. Snoke and S. Stringari, *Bose-Einstein Condensation Cambridge Univ*, 1995
(cit. on pp. 38, 56).

[94] M. Szymańska, J. Keeling and P. Littlewood,
Nonequilibrium quantum condensation in an incoherently pumped dissipative system,
Physical review letters **96** (2006) 230602 (cit. on p. 38).

[95] T. Lappe, *Non-Markovian Dynamics of Open Bose-Einstein Condensates*, (2021)
(cit. on p. 41).

[96] A. E. Siegman, *Lasers university science books*, Mill Valley, CA **37** (1986) 169
(cit. on p. 56).

[97] F. Brennecke et al.,
Real-time observation of fluctuations at the driven-dissipative Dicke phase transition,
Proceedings of the National Academy of Sciences **110** (2013) 11763 (cit. on p. 57).

[98] N. Takemura, J. Omachi and M. Kuwata-Gonokami, *Fast periodic modulations in the photon correlation of single-mode vertical-cavity surface-emitting lasers*,
Physical Review A **85** (2012) 053811 (cit. on p. 57).

[99] J. Berner et al., *Oscillating modes of driven colloids in overdamped systems*,
Nature communications **9** (2018) 1 (cit. on p. 57).

[100] A. Valencia et al., *Two-photon imaging with thermal light*, Physical review letters **94** (2005) 063601 (cit. on p. 59).

[101] J. Mika et al., *Generation of ideal thermal light in warm atomic vapor*, New Journal of Physics **20** (2018) 093002 (cit. on p. 59).

[102] B. Roussel, P. Degiovanni and I. Safi, *Perturbative fluctuation dissipation relation for nonequilibrium finite-frequency noise in quantum circuits*, Physical Review B **93** (2016) 045102 (cit. on p. 59).

[103] P. Février and J. Gabelli, *Tunneling time probed by quantum shot noise*, Nature communications **9** (2018) 1 (cit. on p. 59).

[104] H. A. M. Leymann et al., *Pump-power-driven mode switching in a microcavity device and its relation to bose-einstein condensation*, Physical Review X **7** (2017) 021045 (cit. on p. 59).

[105] A. Posazhennikova, M. Trujillo-Martinez and J. Kroha, *Thermalization of Isolated Bose-Einstein Condensates by Dynamical Heat Bath Generation*, Annalen der Physik **530** (2018) 1700124 (cit. on p. 59).

[106] R. Nyman and J. Marelic, *Experimental evidence for inhomogeneous pumping and energy-dependent effects in photon Bose-Einstein condensation*, () (cit. on p. 59).

[107] S. Greveling, K. Perrier and D. van Oosten, *Density distribution of a Bose-Einstein condensate of photons in a dye-filled microcavity*, Physical Review A **98** (2018) 013810 (cit. on p. 59).

[108] D. L. Goodstein, *States of matter*, Courier Corporation, 2014 (cit. on p. 60).

[109] N. P. Proukakis, D. W. Snoke and P. B. Littlewood, *Universal themes of Bose-Einstein condensation*, Cambridge university press, 2017 (cit. on p. 60).

[110] M. Andrews et al., *Observation of interference between two Bose condensates*, Science **275** (1997) 637 (cit. on p. 60).

[111] M. Toda et al., *Statistical physics II: nonequilibrium statistical mechanics*, vol. 2, Springer Science & Business Media, 1991 (cit. on p. 60).

[112] M. Yamaguchi et al., *Second thresholds in BEC-BCS-laser crossover of exciton-polariton systems*, Physical review letters **111** (2013) 026404 (cit. on p. 60).

[113] E. Kammann et al., *Crossover from photon to exciton-polariton lasing*, New Journal of Physics **14** (2012) 105003 (cit. on p. 60).

[114] D. Dung et al., *Variable potentials for thermalized light and coupled condensates*, Nature Photonics **11** (2017) 565 (cit. on p. 60).

[115] C. Kurtscheid et al., *Thermally condensing photons into a coherently split state of light*, Science **366** (2019) 894 (cit. on p. 60).

[116] V. N. Gladilin and M. Wouters, *Vortices in nonequilibrium photon condensates*, Physical Review Letters **125** (2020) 215301 (cit. on p. 60).

[117] V. N. Gladilin and M. Wouters,
Vortex unbinding transition in nonequilibrium photon condensates,
arXiv preprint arXiv:2104.13203 (2021) (cit. on p. 60).

[118] R. Ma et al., *A dissipatively stabilized Mott insulator of photons*, Nature **566** (2019) 51 (cit. on p. 60).

[119] M. Vretenar et al., *Controllable Josephson junction for photon Bose-Einstein condensates*, Physical Review Research **3** (2021) 023167 (cit. on p. 60).

[120] M. Vretenar, C. Toebes and J. Klaers,
Modified Bose-Einstein condensation in an optical quantum gas,
arXiv preprint arXiv:2105.10708 (2021) (cit. on p. 60).

[121] Y. Lin et al.,
Dissipative production of a maximally entangled steady state of two quantum bits,
Nature **504** (2013) 415 (cit. on p. 60).

[122] M. P. Hokmabadi et al.,
Non-Hermitian ring laser gyroscopes with enhanced Sagnac sensitivity,
Nature **576** (2019) 70 (cit. on p. 60).

[123] L. J. Fernández-Alcázar, R. Kononchuk and T. Kottos,
Enhanced energy harvesting near exceptional points in systems with (pseudo-) PT-symmetry,
Communications Physics **4** (2021) 1 (cit. on p. 60).

APPENDIX A

Appendix

A.1 The limits a high photon count on the streak camera imposes on the time delay

In the streak camera measurement scheme, the exact positioning of the photon detection events on the time-axis is critical for the accurate measurement of time-resolved photon correlations. The main error source in this technique is the determination of the photon positions on each frame (see also ref. [70]). An algorithm built-in the streak camera determines the position of each detection event during the measurements. However, each photon detection may excite more than one adjacent pixels on the CCD chip. Therefore, the determination of the exact photon position is less precise when photons hit pixels that are closely located on the chip. This technical limitation causes a systematic error on the measured second order correlation functions for small time delays.

To identify the systematic error caused by the inaccurate positioning of the photons, we measured the second order correlation function of a coherent source (HeNe laser) where a measurement of $g^{(2)}(t) = 1$ is expected for all times t. From the deviations of $g^{(2)}(t)$ from this value at small times, we identified the limits on the delay time introduced by this technical limitation. The systematic feature introduced by the inaccurate photon positioning becomes more prominent when there are more photon-detection events on the frames. We repeated the measurements for different intensity levels on the camera. In this way, we determined the dependence of this systematic error to the number of detected photons pairs per frame. We did not include the predetermined region with the systematic error in our further analysis for the study of the fluctuation dissipation relations (see Figure A.1).

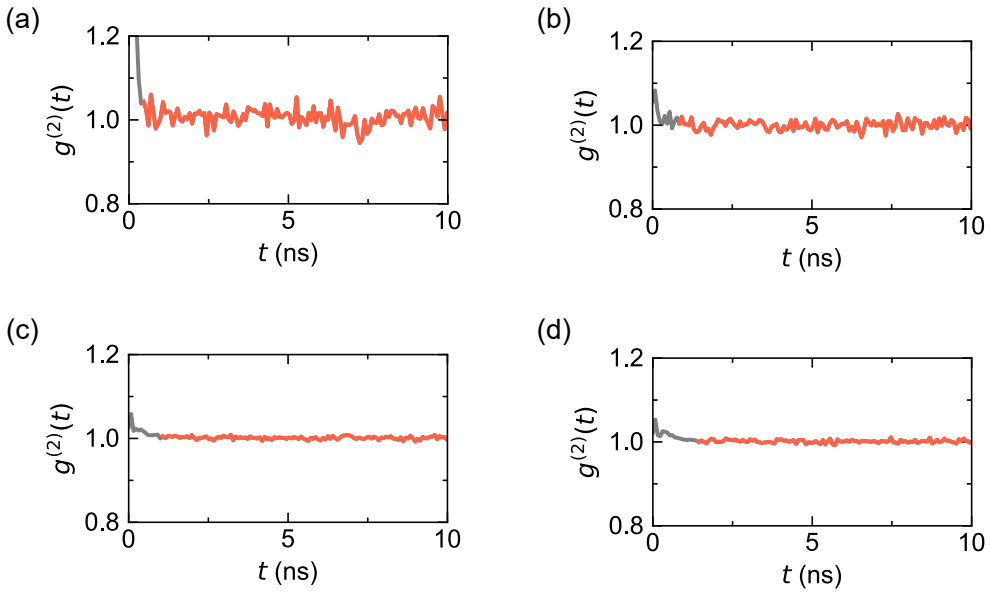

Figure A.1: Measured second-order correlation functions, $g^{(2)}(t)$ of a HeNe laser. The gray regions in the curves show a systematically added feature at small times t due to the inaccurate photon positioning of the streak camera. The effect depends on the intensity of detected light on the streak camera. (a) When the photon count at each frame is small, the effect is limited to a small number of adjacent pixels. Photon pairs per pixel ≈ 0.002. Feature width in time: 6 pixels, corresponding to the first 0.45 ns. (b) Photon pairs per pixel ≈ 0.03. Feature width in time: 11 pixels, corresponding to the first 0.8 ns. (c) Photon pairs per pixel ≈ 0.07. Feature width in time: 14 pixels, corresponding to the first 1.05 ns. (d) Photon pairs per pixel ≈ 0.11. Feature width in time: 19 pixels, corresponding to the first 1.4 ns.

APPENDIX B

Appendix

B.1 Additional data and the experimental parameters

Experimental parameters and fit results for the five different data sets given in the non-Hermitian phases (Figure 3.4).

Data set	κ (GHz)	$\sigma\kappa$	M	σM
1	2.2	0.19	$4.76 \cdot 10^9$	$2.9 \cdot 10^7$
2	1.7	0.04	$6.53 \cdot 10^9$	$5.5 \cdot 10^6$
3	2.6	0.06	$4.08 \cdot 10^9$	$1.4 \cdot 10^8$
4	2.5	0.11	$2.04 \cdot 10^9$	$3 \cdot 10^7$
5	2.7	0.31	$1.83 \cdot 10^9$	$2.4 \cdot 10^7$

Table B.1: The loss rate κ and the total molecule number M, determined from the fits of the oscillation frequency Ω_0 and decay times $\tau_{1,2}$

Data set	$\Delta(\hbar/k_B \cdot T)$	λ_c (nm)	B_{abs} (Hz)	B_{em} (kHz)	κ_{th} (GHz)
1	$4.4 \cdot 10^9$	571.3	420	23.9	2.3
2	$6.3 \cdot 10^9$	570.4	490	24.5	2.2
3	$4 \cdot 10^9$	570.4	490	24.5	2.2
4	$1.9 \cdot 10^9$	570.4	490	24.5	2.2
5	$1.7 \cdot 10^9$	575	219	21.7	3

Table B.2: The measured values of the cutoff wavelength λ_c, and calculated values of the dye-cavity detuning Δ. The Einstein coefficient for emission B_{em} can be determined from the quoted Einstein coefficient for absorption B_{abs} for the corresponding wavelength using the Kennard–Stepanov relation. The theoretical loss rate of the cavity κ_{th} is calculated for the theoretical reflectivity curves from the supplier of the cavity mirrors.

List of Figures

List of Tables